Poro-perm relations of Mesozoic carbonates and fault breccia, Araxos Promontory, NW Greece

Sergio C. Vinciguerra[1], Federico Vagnon[2], Irene Bottero[1], Jerome Fortin[3], Angela Vita Petrullo[4],

Dimitrios Spanos[5], Aristotelis Pagoulatos[5], Fabrizio Agosta[4,6]

[1]Department of Earth Sciences, University of Turin, Turin, 10125, Italy

[2]Department of Environment, Land and Infrastructure Engineering, Politecnico di Torino, Turin, 10129, Italy

[3]Laboratoire de Géologie - Ecole Normale Supérieure/ CNRS UMR8538, PSL Research University, Paris, 75005, France

[4]GeoSMART Italia s.r.l.s, Potenza, 85100, Italy

[5] Hellenic Petroleum, Athens, 15125, Greece

[6] Department of Science, University of Basilicata, Potenza, 85100, Italy

Correspondence to: Sergio C. Vinciguerra (sergiocarmelo.vinciguerra@unito.it)

Abstract. Aiming at assessing the porosity and permeability properties, we present the results of microstructural and laboratory measurements of density, porosity, V_P, V_S, and electrical resistivity performed in dry and in saturated conditions on 54 blocks of Mesozoic carbonate host rocks and fault breccias. Host rocks consist of carbonate mudstones, wackestones, packstones, and sedimentary breccias pertaining to the Senonian and Vigla formations. These rocks show average density values, low values of porosity, and medium-to-high P- and S-wave velocities. Fault breccias derive from high-angle extensional and strike-slip fault zones, and are characterized by a wider range of density, porosity values up to 5-10 times higher than host rock, and low ultrasonic velocities. Independently on lithology, the carbonate host rocks might include vugs due to selective dissolution. Differently, the fault breccia samples include microfractures. A slight textural anisotropy is documented in the carbonate host rocks, whereas a higher degree of anisotropy characterizes the fault breccias. Selected samples were also tested in pressure vessels with confining pressure up to 80MPa, showing that transport properties along microcracks in fault breccias can significantly increase with increasing depth. In order to assess rock permeability and porosity-permeability relations, three different protocols are employed. Two of them are based on the Effective Medium Theory, so that permeability is computed by inverting ultrasonic measurements and assuming an array of penny-shaped cracks embedded in an impermeable host matrix. Accordingly, the aspect ratio and crack width are obtained by the seismic measurements. Two end terms have been modelled by assuming all cracks isolated, and unconnected or all cracks connected into the network. Application of these two protocols shows a systematic variation of permeability with porosity, whereas the results of the third one, based on the digital image analysis outcomes, do not exhibit systematic variation. We interpret this behavior as due to the not-selective dissolution of the outcropping carbonates causing a wide range of measured fracture aperture values.

1 Introduction

Geophysical exploration methods employed for the analysis of potential reservoirs of geofluids commonly consist of seismic survey, gamma ray logging, stress field detection survey, controlled source electromagnetic data surveys and

many others. Usually, petrophysical analyses are performed on well logs or on undisturbed core samples directly retrieved from wells. However, before subsurface investigations, laboratory and on-field measurements are performed on outcropping analogs of deep reservoirs, in order to identify fractures and faults and their role on transport properties (Simmons and Cooper, 1978; Walsh, 1965). It is known that isolated fractures such as cracks (joints for geologists) make

40 rocks more compliant, and that connected cracks make rocks more permeable and anisotropic when aligned to each other (Nelson, 2001). The superposition of multiple deformation mechanisms over extended periods of time may therefore give rise to a complex rock fabric, which in turn makes the task of interpreting field-scale seismic surveys highly challenging, unless a priori knowledge of the physical state of the rock is known and understood. The rock fabric is also affected by the diagenetic processes (Laubach et al., 2010; Bailly et al. 2019a,b, 2022), which in carbonates involves the occurrence

45 of physical/chemical compaction and pervasive cementation (Ferraro et al. 2019).

At a larger scale, fault zones in cemented carbonates, might provide a significant control on both storage and transport fluid properties (Ferraro et al., 2020). Considering that fault zones often include fault cores (FC's) made up of fault rocks and main slip surfaces, and fault damage zones (DZ's) consisting of fractured carbonates crosscut by small, subsidiary faults (Agosta and Aydin, 2006; Giuffrida et al., 2019), they form combined barrier-conduit permeability structures (Caine

50 et al., 1996) in which the low permeability FC's are flanked by FZ's enhancing the fault-parallel fluid flow (Rawling et al., 2001; Ferraro et al., 2018; Volatili et al., 2022). In case of un-cohesive and permeable fault rocks, FC's also conduce fluids so that the entire fault zones may form distributed fluid conduits (Caine et al., 1996; Agosta et al., 2021).

The permeability estimation of both FC's and DZ's is however a complex task to accomplish due to the heterogeneity and anisotropy of rock masses (Piscopo et al., 2018). Because of the difficulties of in situ measurements, a large number

55 of theoretical models has been proposed to predict the change of one property of cracked rocks from the measurement of another property (Benson et al., 2006). However, in order to apply anyone of these models, it is necessary to verify them by performing systematic control experiments in which all the relevant properties are measured on the same sample under the same experimental conditions. Such an approach has the advantage of eliminating possible errors caused by the presence of depositional and structural heterogeneities forming prominent anisotropies within carbonate rocks. To date,

60 such systematic studies have been rare.

In this work, we focus on the petrophysical characterization of rock samples collected from the Araxos Promontory, western Greece. The area of western Greece, which is characterized by presence of major petroleum systems extending onto the Ionian Sea (Karakitsios, 2013) has been the subject of recent studies documenting the sedimentary infill of the Ionian Basin (Bourli et al., 2019a, b), and of their tectonic evolution (Tavani et al., 2019, Smeraglia et al., 2023). Aiming

65 at defining the poro-perm relations for both host and fault rocks, we investigate a variety of carbonate lithofacies by integrating the results of 2D image and petrophysical analyses in order to first compute the values of permeability, and then compare the results with those after experimental measurements. Results are discussed in light of the direct observation of the connected pore space, so that a protocol for petrophysical carbonate analysis is presented. Results might be applied elsewhere to many geo-engineering applications. In fact, CO_2 storage in fractured carbonate reservoirs,

70 production of geothermal energy from low-middle enthalpy sites, and preservation of deep aquifers during production of fossil energies could be some of the possible applications of the proposed protocol.

2   Geological setting

The Araxos Promontory pertains to the External Hellenides, Greece (Figure 1), and consists of a fold-thrust belt, ftb, that formed in response to the convergence between the Apulian margin and the Internal Hellenides (Pelagonian)

75   microcontinent (Chatzaras et al., 2006; Doutsos et al., 1993; Mountrakis, 1986; Xypolias and Koukouvelas, 2005). At a larger scale, the study area is part of the Dinarides-Albanides-Hellenides orogenic belt, which formed as a consequence of the Cenozoic collision between the Adria-Africa and Eurasian continental plates (Papanikolaou, 2021; Robertson and Shallo, 2000; Roure François et al., 2004; Underhill, 1989). Such a collisional tectonics was subsequent to the subduction of the oceanic crust interposed between the two aforementioned continental plates (Robertson et al., 1991; Saccani et al.,

80   2003). The Hellenides ftb is made up of four main structural domains, which respectively consist of from west to east (Figure 1a): (i) Apulian carbonate platform, (ii) Ionian pelagic basin, (iii) Gavrovo carbonate platform, and (iv) Pindos oceanic basin (Karakitsios, 2013b; Underhill, 1989). These structural domains were tectonically juxtaposed during the late Eocene-Miocene, piggy-back thrusting tectonics (Robertson and Dixon, 1984). Occasional out-of-sequence thrusting also took place (Sotiropoulos et al., 2003). Currently, the outer domain of the Hellenides ftb is subjected to an active

85   compression, as documented by (Kiratzi and Louvari, 2003) and Jolivet and Brun (2010).

At a smaller scale, the Araxos Promontory is located in the Ionian zone of the Hellenides ftb, which includes large parts of some Ionian islands, the Epiros, the Akarnania, and the western part of Peloponnesus. The Ionian zone is bounded by the NW-SE to NNW-SSE striking Ionian thrust, to the west, with the pre-Apulian zone forming the footwall block, and by the NNW-SSE striking Gavrovo thrust, to the east (Figure 1a). Specifically, the Araxos Promontory lies in the Internal

90   Ionian Zone, east to the Gavrovo thurst, and is also bounded northward by the roughly WNW striking and seismically active normal faults of the Gulf of Patras and Corinth (Figure 1a), a seismically active region associated to crustal stretching and extension (Jolivet et al., 2015).

The Araxos Promontory, which is flanked by Holocene continental deposits both eastward and southward, is made up of an E-SE dipping carbonate monocline including Lower Cretaceous, chert-bearing, deep-water limestones (Danelian et

95   al., 2018; Skourtsis-Coroneou et al., 1995), and Upper Cretaceous-Eocene pelagic and hemipelagic limestones with frequent calciturbidites and sedimentary breccias interlayers (Bourli et al., 2019a; Karakitsios and Rigakis, 2007). The latter breccias and calciturbidites are made up of Vigla-derived clasts, and with minor intercalations of thinly bedded pelagic limestones. The whole Cretaceous-Eocene carbonate succession overlies remnants of up-faulted Lower Jurassic carbonate blocks. The former rocks form the post-rift sequence postdating the Triassic-early Jurassic pre-rift sequence,

100   the early Jurassic-Late Jurassic syn-rift sequence, and the post-rift sequence (Karakitsios, 2013). A detailed lithostratigraphic representation of the Ionian carbonates is reported in Figure 1b. We note that a more recent work assessed that the Triassic-early Jurassic succession is also part of the syn-rift sequence (Stampfli, 2005). Altogether, the pre-, syn-, and post-rift sequences were later deformed during thrusting tectonics by mean of NNW-SSE striking thrust faults and folds, which altogether determined a WSW-ENE shortening direction (Tavani et al., 2019; Underhill, 1989).

105   Smaller scale folds associated to a N-S shortening direction were also documented east of the Lefkada Island, and throughout the Hellenides, as well as in the Araxos Promontory itself (Smeraglia et al., 2023).
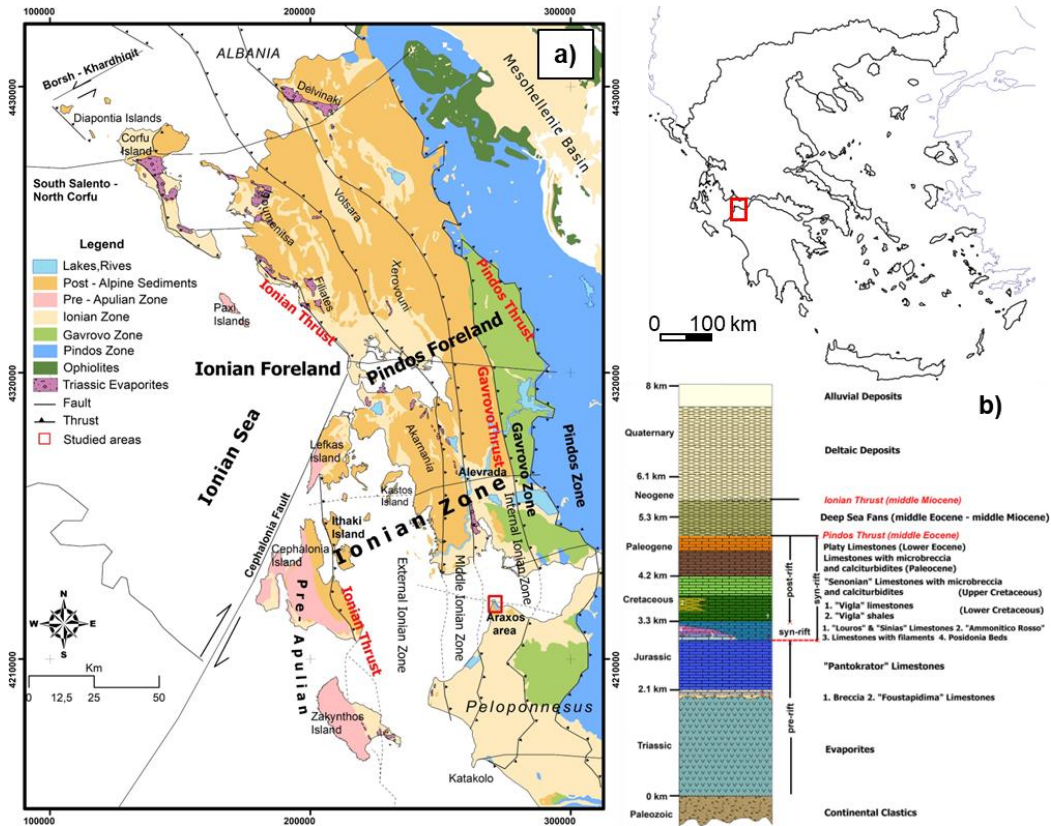
Figure 1: a) Geological sketch of the Western Greece and b) lithostratigraphic column of the Ionian zone (modified from (Bourli et al., 2019).

3 Methods

3.1 Sampling strategy and classification

Six to ten cm-sided cubes and parallelepipeds, hereafter named as rock blocks, were saw-cut from the hand specimens collected in the field. We employed these rock block to perform experimental analyses aimed at measuring the values of porosity, density, ultrasonic velocities and electrical resistivity at room pressure and temperature. In the field, the hand specimens were collected because representative of the following carbonate lithologies (Woodcock and Mort, 2008):

- Host Rocks exposed Away from major Fault Zones (HR-AFZ);
- Host Rocks in Proximity to Fault Zones (HR-PFZ);
- Fragmented Host Rocks from Fault Zones (FHR-FZ);
- Crush Fault Breccia from Fault Zones (CFB-FZ);
- Fine Crush Fault Breccia and fault microbreccia from Fault Zones (FCFB-FZ).

3.2 Microstructural analyses

For rock texture digital analysis, 44 rock slabs obtained from the same hand specimens employed for petrophysical
analyses were selected for microstructural analysis. The rock slabs were saw cut either parallel or perpendicular to
bedding/slip surfaces. Each rock slab was manually smoothed in order to later acquire good digital images, and then
scanned by using high-resolution, 2400 dpi scanner. As a result, a detailed textural analysis was conducted aiming at
assessing the main rock textures, as well as the shape, size, sphericity, and roundness of both clasts (host rock samples)
and survivor grains (fault-related samples). Afterward, on the basis of a preliminary qualitative analysis, a discrete 1 cm^2-
wide area was selected from the individual textures documented in single rock slabs to perform quantitative image
analysis. This means that rock slabs with only one main texture were analyzed by selecting only 1cm^2 area, whereas those
with multiple textures were analyzed by selecting multiple 1cm^2 areas. In all cases, cm-sized clasts/grains were avoided.
The digital images were processed by using both Gimp and ImageJ software applications. Employing the former software,
the selected 1cm^2 areas were analyzed in order to identify all visible clasts (hos rocks)/survivor grains (fault rocks). The
individual clasts/survivor grains were then manually drawn in order to carefully trace their individual shapes. As a result,
a bitmap image was obtained for the single 1cm^2 areas. There, the clast/survivor grains were reported with a black color,
while both carbonate matrix and cement with a white color (Figure 2a). Pores were not considered at this stage of the
work.

Afterwards, by using the command "Analyze Particles" of ImageJ software (Figure 2a), all clasts/survivor grains included
in the 1 cm^2 bitmap images were automatically processed to measure: (i) particle count, (ii) total particle area, (iii) average
particle size, (iv) area fraction representative of the percentage of clasts/survivor grains (pixels highlighted in black using
the Threshold command), (v) percentage of matrix, and (vi) perimeter of the clast/survivor grains. A particular attention
was paid to the computation of the Box-counting Dimension $D_{0(grains)}$, which was obtained by using the ImageJ software.
This software automatically superimposed a square grid on each binary image, and then counted the boxes occupied by,
at least, one clast/survivor grain (filling frequency). The procedure was repeated for increasing box sizes. In fact, ten box
classes varying from 2 to 128 pixels were considered for each digital image. As a result, the number of boxes containing
clasts/survivor grains were first computed, and then plotted in a log-log space (Figure 2b). In these plots of box size vs.
number of counts, the latter number reported the boxes with, at least, one portion of a clast/survivor grain. If the spatial
pattern of the clasts/survivor grains was fractal, the plots of the box size versus the filling frequency was described by a
power-law function (Mandelbrot, 1985; Falconer, 2003). Accordingly, the angular coefficient of the best fit line
represented the D_0 value. Specifically, D_0 is equal to the ratio between log N (N: number of boxes including the given
object) and log r (r: inverse of the box size).

The box-counting technique is one of the most common methods used to obtain the fractal dimensions of a pattern. In
particle analysis, the box-counting dimension has a physical meaning similar to that of the fractal dimension (D) related
to grain size distributions. However, the former parameter also contains information on the clast/survivor grains/rock
fragment and matrix/cement ratio, and on both shape and distribution of the clasts/survivor grains/rock fragments. The
fractal dimension, D, is generally determined after a grain-size analysis performed by applying the well-known sieving
procedure to rock samples, which unfortunately implies their disaggregation. This means that the sieving procedure is
responsible for the loss of information regarding the textural relationships of the original samples (Sammis et al., 1987).
The sieving technique hence provides suitable results for near-rounded shapes of grains, but digital image analysis is
preferred in the case of cohesive rocks (Ferraro et al., 2018).
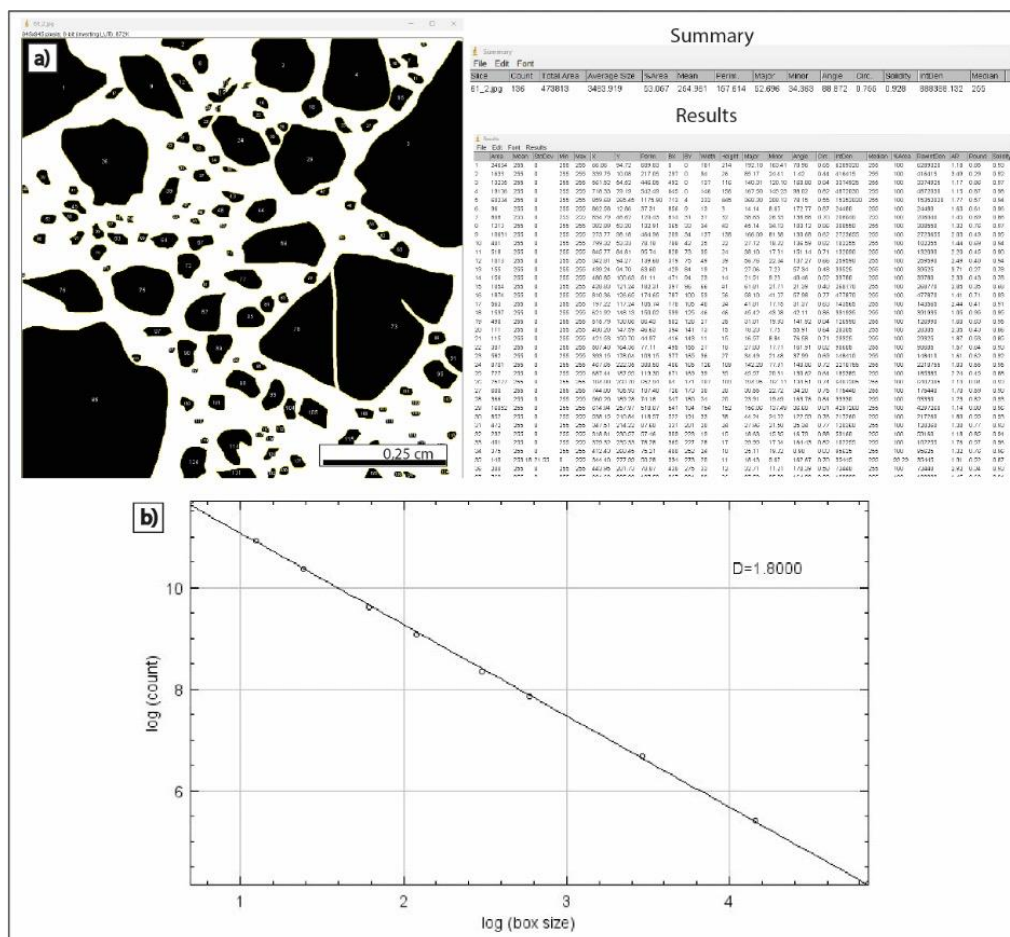
Figure 2: a) Example of image analysis processing carried out with the ImageJ software. In the bitmap image the surviving grains or clasts are black, while the carbonate matrix, cements and pores are white. b) Example of a box size vs. number of counts plot, in a log-log space, which allows computation of the box-counting fractal dimension, D0, which represents the angular coefficient of the best fit line. D0 is therefore equal to the ratio between log N (number of boxes including the given object) and log r (inverse of the box size). We note that the box-counting fractal dimension, D0, is automatically reported as D by the ImageJ software.

From the 44 study rock slabs, 4 x 6.5 cm-wide thin sections impregnated with a blue-dyed epoxy resin were then obtained in order to carry out a pore space digital image analysis. Images of 6.17 x 4.55 mm-wide areas were taken by means of a Nikon Eclipse E600 optical microscope equipped with a Nikon E4500 camera. Afterward, two representative images were selected from each thin section, and then analyzed by using the Gimp and ImageJ software applications. As a result, applying the "select color" command of the Gimp software, the blue portions filled with the epoxy resin were selected. The obtained bitmap images highlighted the pores, shown with a black color, with respect to the clasts/survivor grains/matrix and cement shown with a white color. Then, by using the command "Analyze Particles" of ImageJ software (cf. Figure 3), all black objects (pores) included in the 6.17 x 4.55 mm-wide binary images were automatically counted to compute: (i) 2D porosity (percentage of pixels highlighted in black by using Threshold), (ii) circularity (shape factor, with 1.0 indicating a perfect circle and values close to zero indicating a very elongated shapes), and (iii) aspect ratio (ratio between longest and shortest axes of ellipses inscribed within each pore). The Box-counting dimension, $D_{0(pores)}$ was

180   computed d by superimposing a square grid on the binary image. The automatic counting of the boxes occupied by, at least, one pore was then repeated for increasing box sizes, from 2 to 128 pixels, and finally plotted in a ln-ln space to compute the angular coefficient of the power-law best-fit line. As a result, we obtained the fractal dimension of a pattern, $D_{0(pores)}$, which had therefore a physical meaning similar to that of the fractal dimension related to pore throat distributions (Thompson, 1991; Ferraro et al., 2020).

185
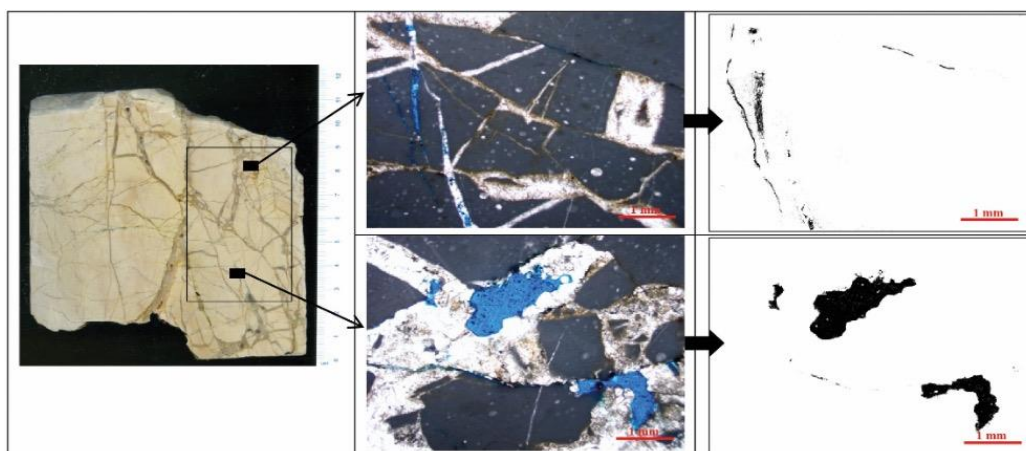
Figure 3: Example of thin sections, in which two representative homogeneous areas of 1 cm2 are highlighted in the enlargements. In the corresponding bitmap image of the enlargement, pores are black, while clast, survivor grains, rock fragments, matrix and cements are white.

190   **3.3   Petrophysical characterization at room pressure and temperature**

3.3.1   Dimensions, weight and volume

The measurement of physical properties such as density, ρ, and porosity, n, provides information on the mechanical characteristics of rocks. The presence of pores in the fabric of a rock material decreases its strength and increases its deformability. Carbonate rocks usually occur with a wide range of porosities, and hence mechanical properties. Since the

195   tested rock blocks were considered with a regular geometry, and consisted of coherent specimens, density and porosity were determined following the "Suggested methods for determining water content, porosity, density, absorption and related properties" of (ISRM, 1979). With this aim, the bulk volume, V, of each specimen was calculated by using the water displacement method. The specimens were saturated by water immersion and repeated shaking (to removing trapped air) for one week. The saturated-surface-dry mass, M_{sat}, was then determined by drying the surface with a

200   moistened cloth, taking care to remove only the surface water, and weighting the samples. The grain mass, Ms, was evaluated in natural condition without drying process in oven in order to avoid any thermal alterations. Porosity and density (under dry, ρ_{dry}, and saturated, ρ_{wet}, sample conditions) were obtained by employing the following equations (1) to (4):

$$\rho_{dry} = \frac{M_S}{V} \qquad (1)$$

205     $$\rho_{wet} = \frac{M_{sat}}{V} \qquad (2)$$

$$n(\%) = \frac{100 \cdot V_v}{V} \qquad (3)$$

$$V_v = \frac{M_{sat} - M_s}{V} \qquad (4)$$

3.3.2 Ultrasonic Pulse Velocity (UPV) measurements

UPV measurements were performed using an ultrasonic pulse generation and acquisition system (Pundit Lab, Proceq).
210 Two Cylindrical 250-kHz tx-rx probes transmitter-receiver (tx-rx) transducers were used for P-wave (V_P) and S-wave (V_S) measurements, along the three orthogonal directions of each block. Measurements were conducted following (ASTM D2845-08, 2008) standard requirements (2008). For each sample, 11 ultrasonic traces were recorded, using a sampling frequency of 2 MHz. Manual picking of the first arrival times of the P-waves and S-waves was performed. The determination of the P- and S- wave ultrasonic velocity was then straightforward as the dimensions of each block were
215 previously measured. The representative velocity of each sample was chosen as the average of the measurements. By employing the following equations (5 to 7), the combined measurement of both P- and S-wave velocities allowed us to retrieve the low-deformation (initial deformation phase of strain-stress curve) elastic parameters (Young modulus, E, shear modulus, G, and Poisson's ratio, ν) from indirect and non-destructive tests:

$$G = \rho \cdot V_S^2 \qquad (5)$$

220
$$\nu = \frac{V_P^2 - 2V_S^2}{2(V_P^2 - V_S^2)} \qquad (6)$$

$$E = 2G(1 + \nu) \qquad (7)$$

3.3.3 Electrical Resistivity (ER) measurements

ER measurements were carried out with a measuring quadrupole connected to a Syscal-Pro (@Iris instruments) acquisition system. The instrumentation consisted of a rubber string with four steel electrodes (2-mm diameter and 40-
225 mm length), equally disposed (3 cm). The electric measurement sequence was based on both Wenner-Schlumberger and Dipole-Dipole quadrupoles. The sequence was repeated 3 times on each block to obtain the apparent resistivity along the same directions used for V_P-V_S determinations. From the ratio between the measured electric potential difference, ΔV, and the injected current, I, the value of apparent resistivity, R_{app}, was obtained as follows:

$$R_{app} = k\,\frac{\Delta V}{I} \qquad (8)$$

230 where k is a geometric factor, depending on the geometry of the adopted quadrupole. For Wenner-Schlumberger and Dipole-Dipole sequences, k is respectively equal to:

$$k = 2 \cdot \pi \cdot a \qquad (9)$$

$$k = n \cdot (n + 1) \cdot (n + 2) \cdot \pi \cdot a \qquad (10)$$

where a is the electrode space of 3 cm, and n is equal to 1 because the electrodes are equally spaced.

3.4 Permeability and UPV measurement at increasing confining pressure

Three samples, two CFB-FZ and one AFZ-HR, were selected and then tested in a pressure vessel at incremental effective pressures up to 80MPa in order to measure permeability and UPV variation. Cylindrical shape samplse with diameter equal to 40 mm and height of 80 mm were cored from the original cubic samples. Measurements were performed at the Laboratoire de Géologie of Ecole Normale Superiure in Paris with a gas permeameter at different confining pressure steps
240 (0.5, 2, 5, 10, 20, 40, 60, 80MPa), in order to guarantee a gradual and progressive closure of the voids space.

Permeability measurements were performed using the constant flow method under a fixed pressure gradient for permeability $> 10^{-2}$ mD and by using the pulse decay method (PDM), for permeability $< 10^{-2}$ mD. The PDM method is based on the transient state induced in a porous media when the equilibrium state is perturbed by suddenly setting a pressure gradient in the sample. Typically, the upstream pressure (P_u) is increased while downstream pressure (P_d)

245   remains unchanged ($\Delta P_0 = P_u - P_d$). Upon perturbation, both up- and downstream pressures evolve with time ($\Delta P(t)$) following an inverse exponential trajectory (transient state) in their natural seeks for the restoration of an apparent equilibrium condition (i.e. steady state). The time (α) needed by the system to restore the apparent equilibrium condition depends on the dimensions of the sample, its properties, the volumes of the up- and downstream reservoirs (V_u, V_d), the physical characteristics of the fluid, and the applied pressure gradient (ΔP_0).

$$\Delta P(t) = \Delta P_0 \frac{V_d}{V_u + V_d} e^{-\alpha t} \qquad (11)$$

250   Since the time decay α is function of permeability, of dynamic viscosity of the pore fluid at temperature of measurement, the geometric properties of the sample, and the compressive storage of the upstream (C_u) and downstream (C_d) reservoirs, permeability values can be calculated via α for each step of increasing pressure. C_u and C_d are defined as the ratios of the change of fluid volume to the corresponding pore pressure variation (%).

For the UPV measurements, a 250-V pulse with a rise time of 1s was generated and transmitted to 2 Vp and Vs

255   piezoelectric transducers placed at the top of each cylindrical sample. Each piezoceramic converted this electrical pulse into a mechanical vibration that propagated into the medium. Two receiving piezoceramic then converted the received mechanical waveform into an electrical signal that was amplified at 40 dB with a sampling frequency of 50 MHz.

4   Experimental Results

4.1   Microstructural analyses

260   The results of microstructural analyses are shown to document the main rock textures. The study rock slabs include five prevalent textures, which respectively consist of matrix-supported carbonates (both host and fault-related rocks, Figure 4a and b), cement-supported carbonates (fault-related rocks, Figure 4c), clast-supported carbonates (host rocks, Figure 4d), survivor grain-supported carbonates (fault-related rocks, Figure 4e), and fragmented carbonates (host rocks, Figure 4f).
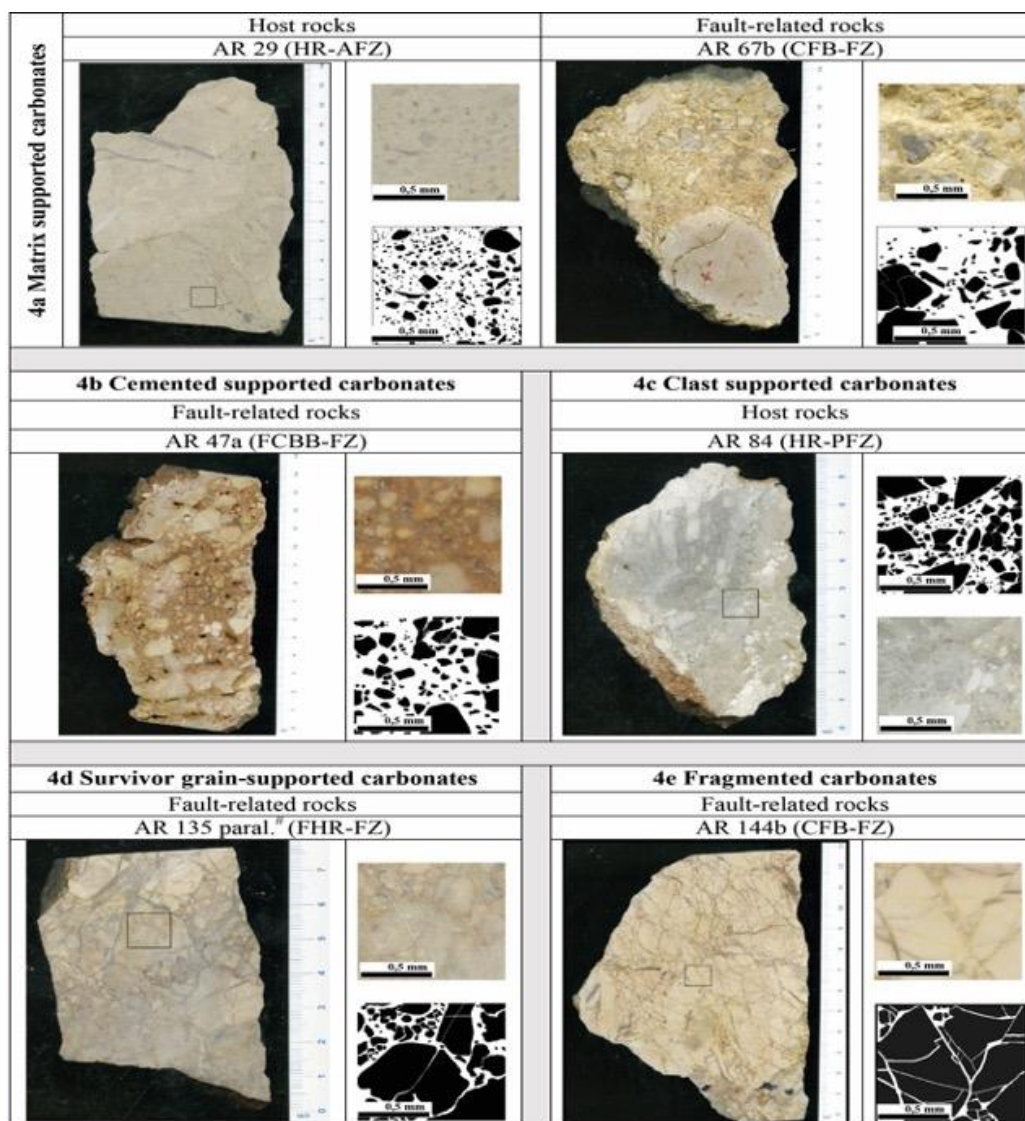
Figure 4: The prevalent textures: a) matrix-supported carbonates (both host and fault-related rocks), b) cement-supported carbonates (fault-related rocks), c) clast-supported carbonates (host rocks), d) survivor grain-supported carbonates (fault-related rocks), and e) fragmented carbonates (fault-related rocks). The black square represents the 1 cm2 selected image for subsequent digital analysis. Upper right: 1 cm2 image for subsequent digital analysis. Bottom right: binary image of the 1 cm2 area. Clasts are in black, the matrix is reported in white.

The 6 host rock samples collected either away from (HR-AFZ) or in proximity to fault zones (HR-PFZ) consist of 4 Senonian limestone and sedimentary breccia samples, and 2 Vigla limestone samples. All samples show the presence of stylolites with some internal porosity, microfractures, and calcite veins. Pores very often align along microfractures, but also form vugs due to not selective dissolution of both clasts and matrix-cements (Figure 5a). The samples show a mean 2D porosity $\leq 0.7\%$, and $D_{0(pores)} \leq 1.15$.

The 5 FHR-FZ samples collected from meso-scale fault zones consist of 1 Senonian limestone (2 rock slabs) collected from a N110E striking Fault Zone, FZ, 1 Senonian limestone collected from a N90E striking fault zone, 1 Senonian sedimentary breccias collected from a N110E FZ, and 1 Vigla limestone collected from a N150E FZ. The samples include microfractures and veins. Pores mainly align along the former structural elements, but both small vugs and large vugs due to not-selective dissolution of both clasts and matrix/cements are also present (Figure 5b). Most of the samples show a mean 2D porosity from ∼ 4.12% to ∼ 7.71%, and $D_0(pores)$ range from ∼ 1.24 to ∼ 1.56; differently, the fractured carbonate packstone is characterized by average values 2D porosity∼0.21%, and a mean $D_{0(pores)}$ equal to 1.4.

The 17 CFB-FZ samples from fault zones consist of 2 samples collected from a N10E FZ, 2 samples from a N20E FZ, 7 samples from a N45E FZ, 3 samples from a N100E FZ, 2 samples from a N110E FZ, and 1 sample from a N130E FZ. The cemented/matrix-supported fault rock textures include vugs due to not-selective dissolution of both clasts and matrix/cements, and pores that often align around the edges of survivor grains (Figure 5c). Most of the samples show a mean 2D porosity ≤ ∼ 3%, with some vlaues≥5, and $D_{0(pores)}$) range from ∼ 0.6 to ∼ 1.62.

The 16 FCFB-FZ samples from fault zones consist of 1 sample collected from a N10E FZ, 2 samples from a N20E FZ, 2 samples from a N45E FZ, 1 sample from a N100E FZ, 8 samples from a N110E FZ, and 2 samples from a N130E FZ. The samples include numerous microfractures and veins. Pores are mainly aligned along the former structural elements. Vugs due to not-selective dissolution of both survivor grains and matrix/cements are present (Figure 5d). The 2D porosity range from ∼ 0.31 to 8.52, and $D0_{(pores)}$ from ∼ 0.91 to ∼ 1.76.
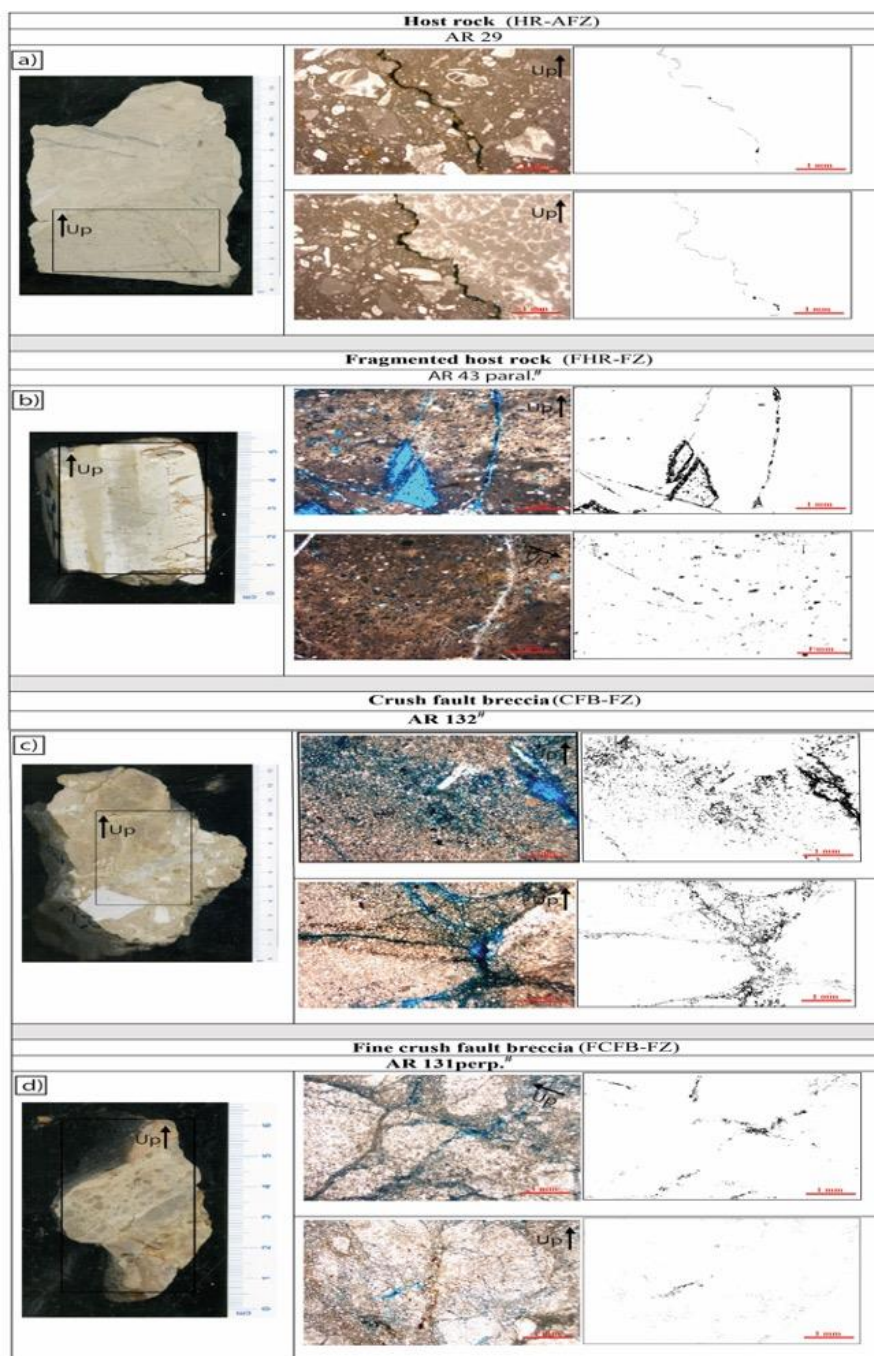
Figure 5: The main pore types documented in a) host rocks, b) fragmented host rock, c) crush fault breccia, d) fine crush fault breccia. The black square on the rock slab represents the thin section area. In the digital images, pores are in black, clasts, matrix and cement in white.

4.2 Petrophysical characterization at room pressure and temperature

300 Figure 6 and Figure 7show density and porosity values measured for each rock sample and their average normalized values for each rock block lithology. In general, density values of both host rocks (HR-AFZ and HR-PFZ) and fractured host rock (FHR-FZ) vary between 2500 and 2900 kg/m³, with porosity values on average lower than 3%. A few samples from the Vigla and Senonian formations show porosity values up to 6%. Differently, CFB-FZ and FCFB-FZ samples show lower values of density, ranging from 2200 to 2900 kg/m³, and higher porosity values. A few samples show porosity

305 values up to 25% due to manmade fracture. Overall, both CFB-FZ and FCFB-FZ samples are quite heterogeneous in terms of petrophysical characteristics depending upon distance from the main slip surfaces and pervasiveness of reddish carbonate cements. In general, density decreases approaching the main slip surfaces (dashed trend lines in Figure 6), whereas porosity increases (dashed trend line in Figure 7).
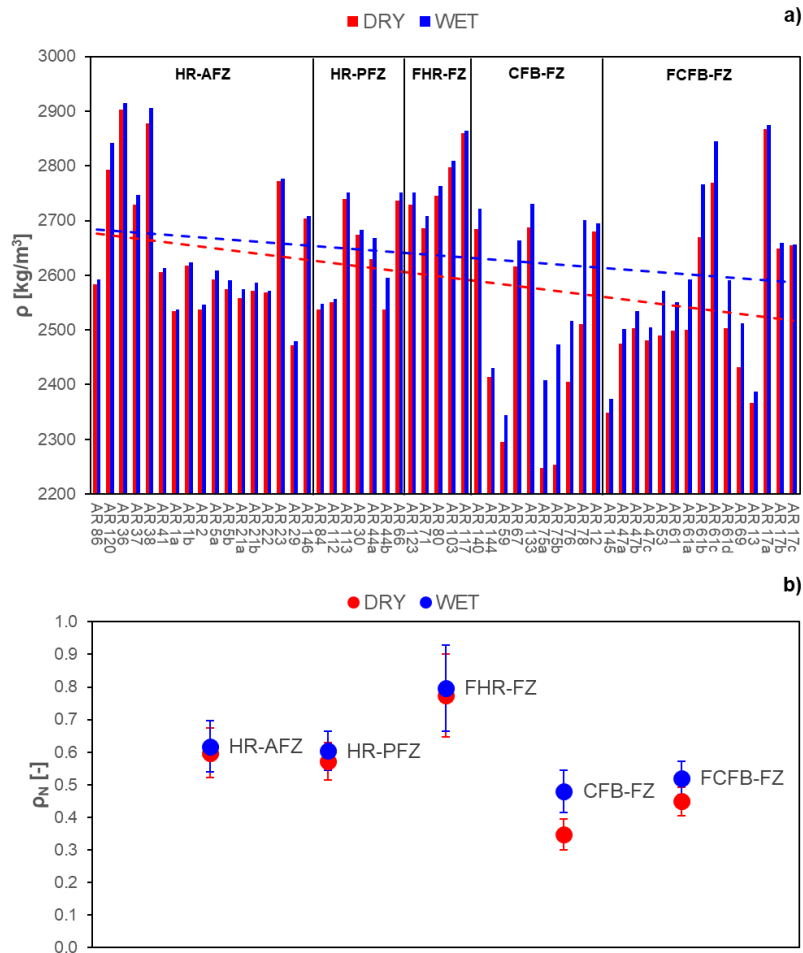
310 **Figure 6: a) Dry (red bars) and saturated (blue bars) density values for all the rock samples and b) average normalized density values for each group of rock collected in the surrounding of the fault zone.**
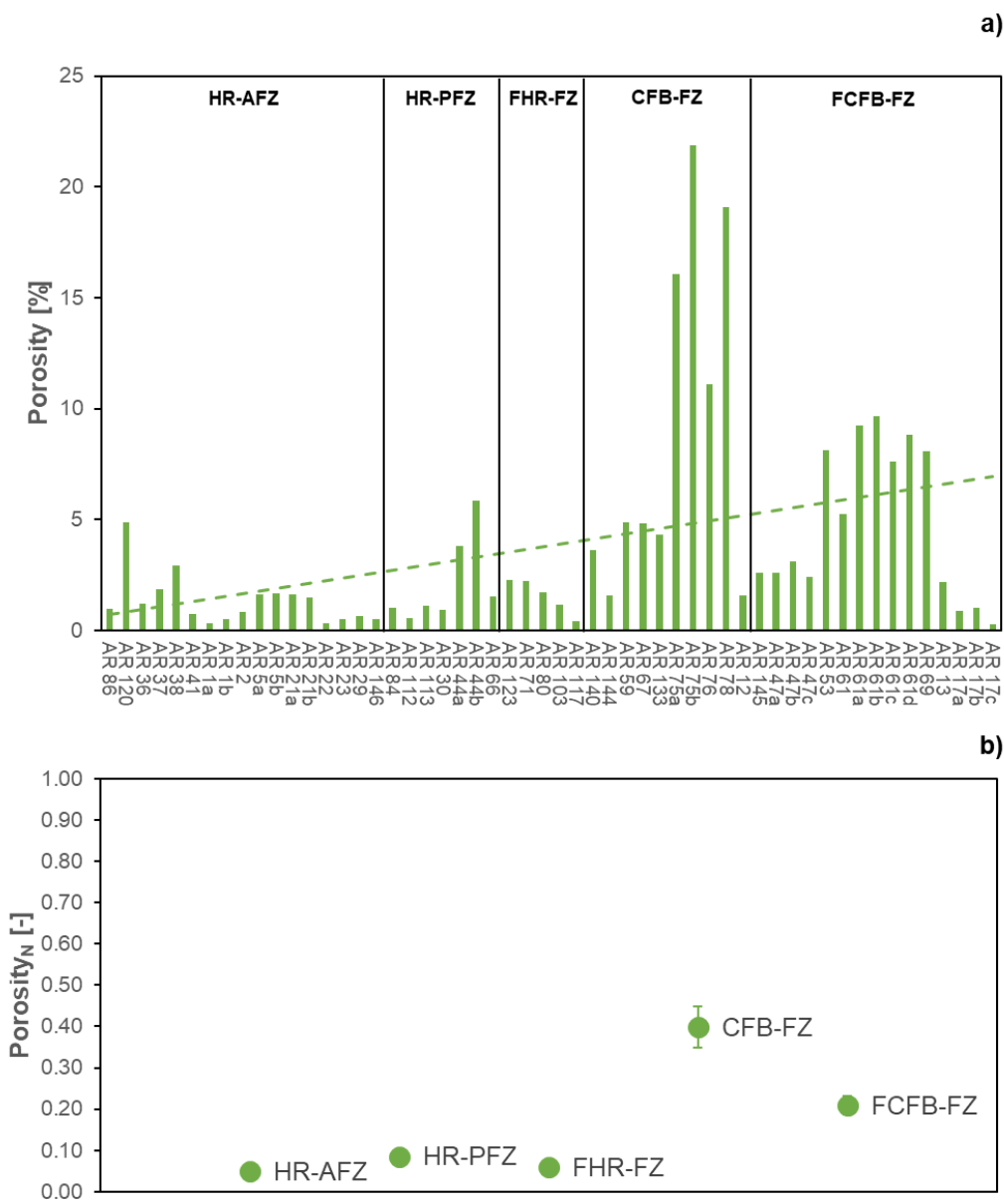
Figure 7: a) Porosity values for all the rock samples and b) average normalized porosity values for each group of rock collected in the surrounding of the fault zone.

UPV measurements were performed both in dry and in saturated conditions on each block dimensions and then averaged to provide a mean normalized value for each sample. Figure 8 and Figure 9 show the V_P and V_S values for each block. V_P values (in dry conditions) vary between 6400 m/s (HR-AFZ) and 2600 m/s (FCFB-FZ). About V_S measurements, the range is comprised between 3600 and 1200 m/s. Considering the aforementioned ultrasonic data, $V_{P\,WET}$ values are always

320   greater than the $V_{P\,DRY}$ values. In general, the difference between V_P in saturated and dry conditions is higher for samples collected closely to fault zones, mirroring the increase in porosity shown in Figure 7. Conversely, the V_S values remain almost unchanged for the two analyzed conditions as shown in Figure 9.
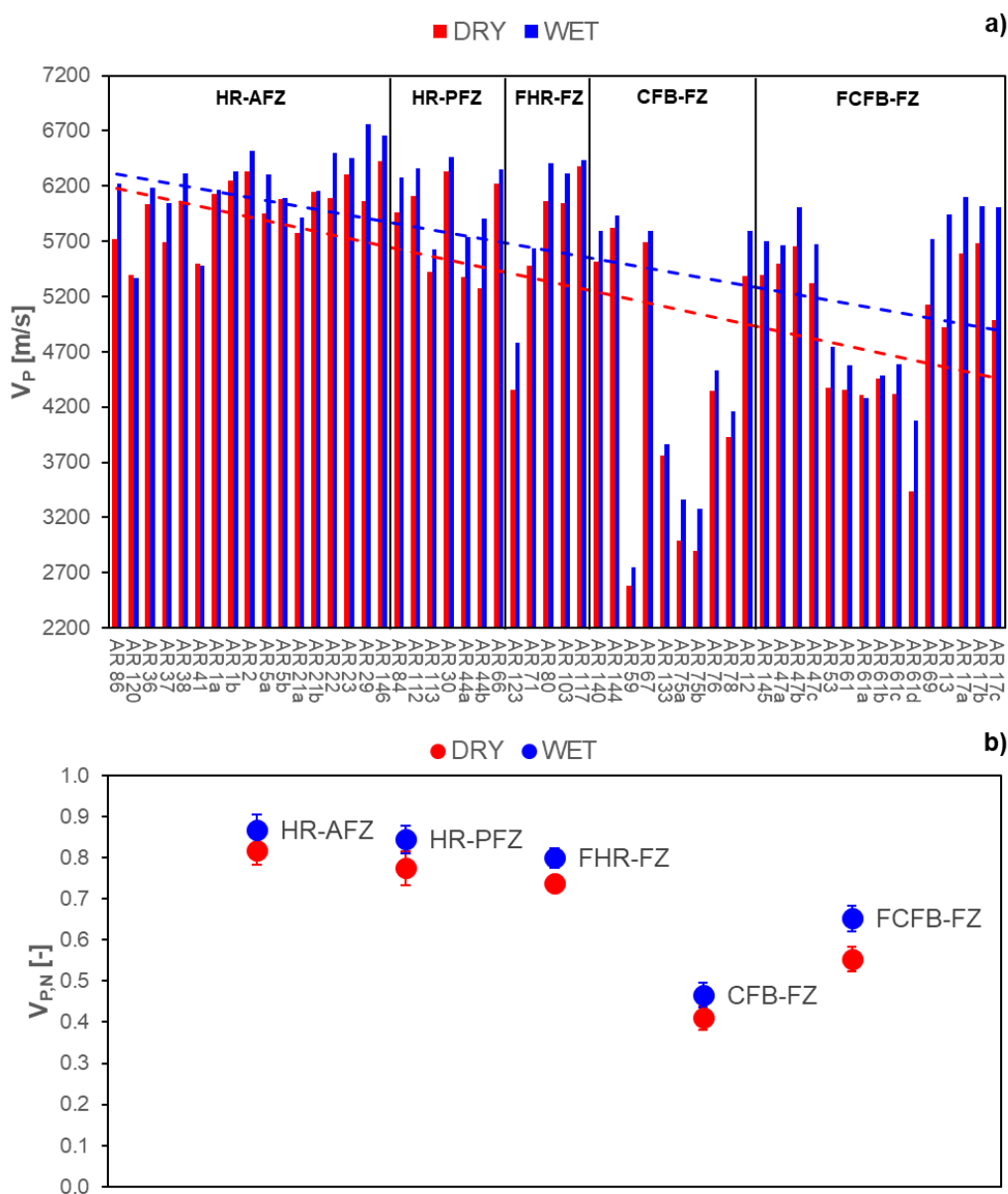
Figure 8: a) V_P values in dry (red bars) and saturated (blue bars) conditions evaluated for each rock sample and b) average normalised values for each rock group.
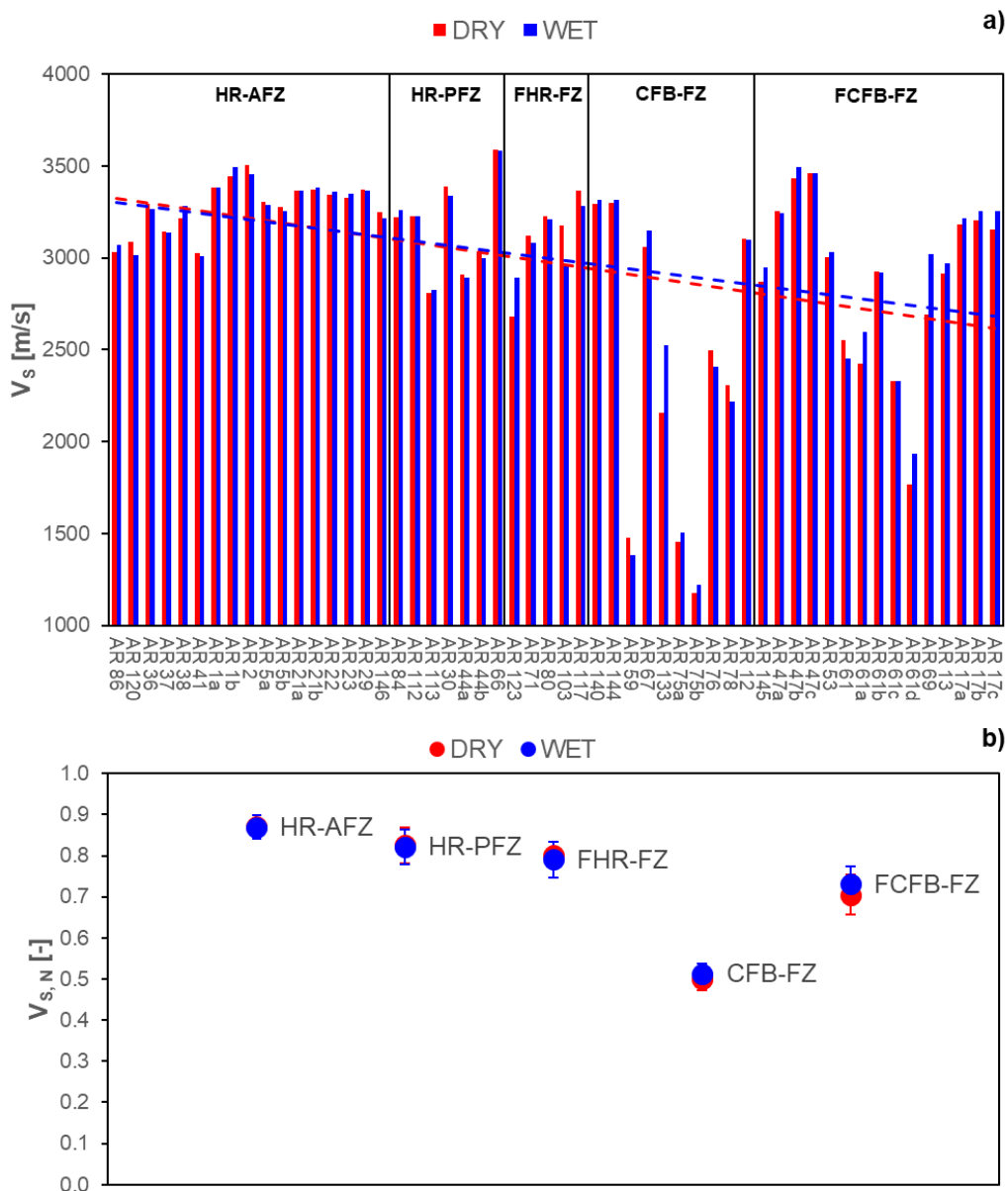
Figure 9: a) VS values in dry (red bars) and saturated (blue bars) conditions evaluated for each rock sample and b) average
330 **values for each rock group.**

Figure 10 shows the amount of textural anisotropy, k, evaluated for V_{Pdry}, V_{Pwet}, V_{Sdry}, and V_{Swet}. k is estimated as following:

$$k = \frac{V_{i_{max}}}{V_{i_{min}}} \qquad (12)$$

335

With V_i is the ultrasonic velocity value (both P and S) in dry or wet conditions.

V_i values were measured either parallel or orthogonal (empty bars) to bedding (HR-AFZ and HR-PFZ) or to main slip surfaces (FHR-FZ, CFB-FZ and FCFB-FZ). There is not a clear directivity in the textural anisotropy. In most cases, the lowest values of velocity correspond to directions orthogonal to the aforementioned heterogeneities, but this trend is not

340 systematic. When this occurs, the other two directions exhibit the same velocity values, consistently with a mono-directional anisotropy. These data are hence interpreted as due to planar heterogeneities (bedding interfaces, fractures sheared fractures, slip surfaces) and not to linear heterogeneities such as elongated minerals.

Overall, the highest k values were observed in the carbonate fault rocks relative to the host rocks. Such a result is consistent with a textural anisotropy profoundly affected by tectonic fractures and slip surfaces.

345 In detail, the k value reaches a value up to 1.2 in HR-AFZ, and up to 1.4 in (HR-PFZ. For the latter rocks, the highest computed values are for blocks AR 113 and AR 44, corresponding to Senonian microbreccia samples collected in proximity to N110E FZ's crosscutting the topmost and bottom portions of the Senonian carbonates, respectively. According to the results of microstructural analysis, these anisotropies are due to mesoscale fractures dissecting the host rock blocks. FHR-FZ samples are also characterized by k values up to 1.2, confirming their close similarities with the

350 previous ones.

Regarding both CFB-FZ and FCFB-FZ, values up to 1.8 (AR 59) and 2.3 (AR 69) are obtained. The AR 59 block derives from a N110E FZ crosscutting the bottom Senonian succession, whereas the AR69 block derives from a small N130E FZ adjacent to the previous one. According to the results of microstructural analysis, these anisotropies can be associated to mesoscale fractures and/or sheared fractures that sub-parallel the main slip surfaces. Regarding the AR75 block, we also

355 note the large difference between AR 75a (k value about 1.3) and AR 75b (k value about1.7) is due to the presence of laterally discontinuous fractures and sheared fractures exposed in the field, which affected the textural anisotropy of study fault breccia.
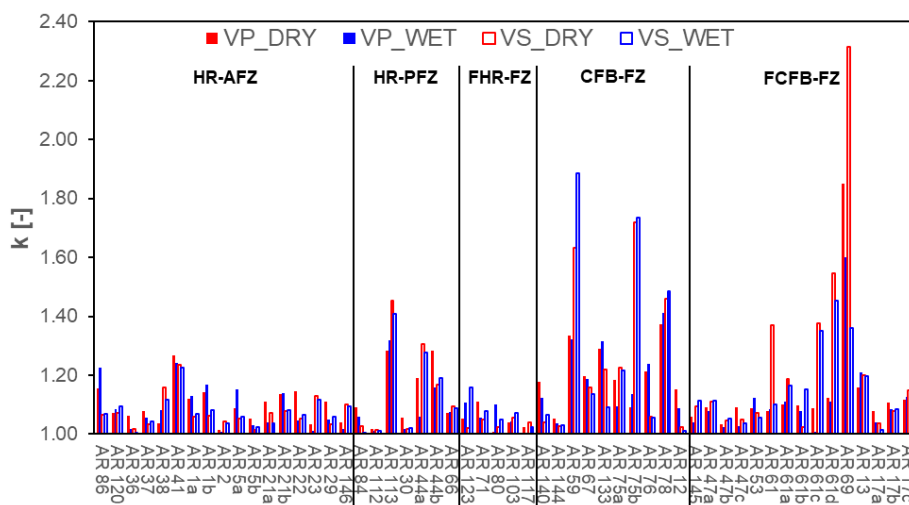
Figure 10: a) V_P values measured along the three directions of the sample blocks. Empty bars represent the direction orthogonal to bedding (for HR-AFZ and HR-PFZ) or slip surfaces (FHR-FZ, CFB-FZ and FCFB-FZ). b) Textural anisotropy degree for all blocks.

360

Dynamics Young modulus and Poisson's ratio were evaluated from seismic values for each studied lithology (Figure 11). We note that the dynamic moduli computed for the host rock blocks (HR-WFZ, HR-PFZ, and FHR-FZ) is higher than

365   those obtained for the fault rock blocks (CFB-FB and FCFB-FZ) mirroring the effect of fracturing (porosity) on their mechanical properties. These values will be useful for an indirect estimation of the crack density evolution at the meso- and site-scale by using the theory proposed by (Nasseri et al., 2007), as it will be discussed in the following.
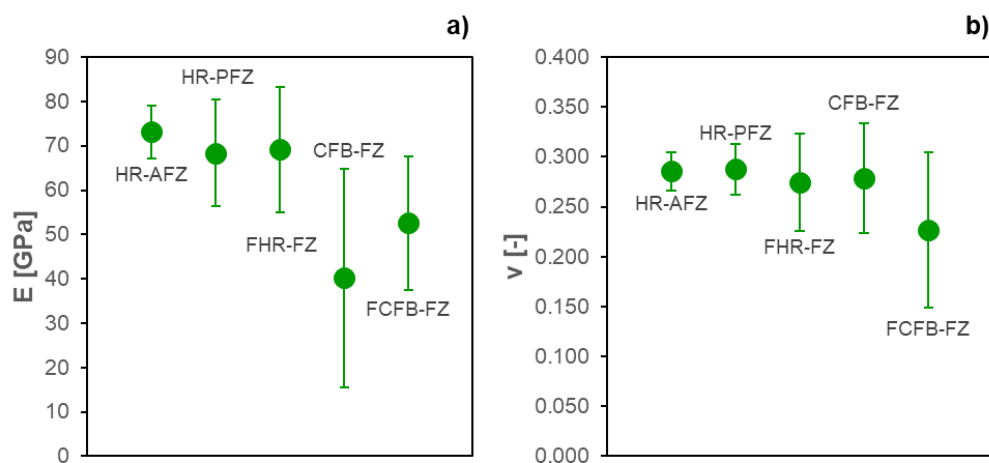
Figure 11: Trend of a) Young's modulus E and b) Poisson's ratio, v calculated from seismic values for each rock lithology
370   **group.**

The Electrical Resistivity (ER) values measured for the carbonate rock blocks are summarized in Figure 12. Data are reported for both for dry and saturated test conditions. A clear change in the electrical properties is documented among the studied lithologies. In fact, the measured R_{DRY} values are higher in fault rock blocks (CFB-FZ and FCFB-FZ) compared to the host rock blocks (HR-AFZ, HR-PFZ, FHR-FZ).

375
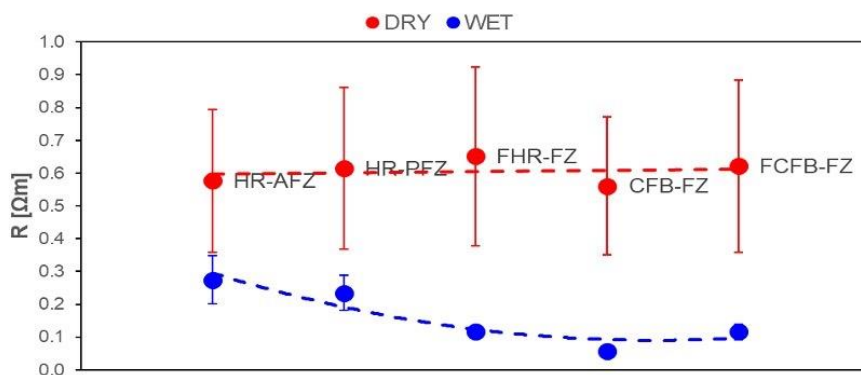
Figure 12: Average normalized resistivity values in dry (red) and saturated (blue) conditions measured for each rock group.

Figure 13 shows the variation of dynamic E (orange bars) and n (green line) for each rock sample as a function of the
380 hypothetical distance from the main slip surfaces characterizing an ideal fault zone. We document a good match between
porosity, that could be intended as a proxy of the degree of fracturing, and the E values; in fact, as porosity increases, the
dynamic modulus decreases in agreement with previous findings (cf. Figure 11).
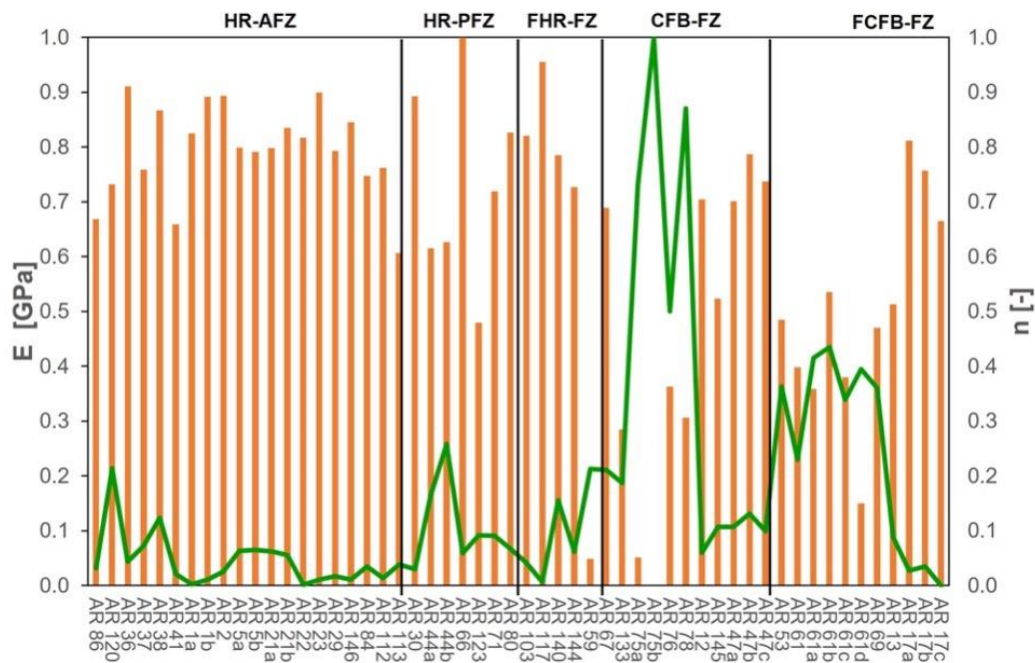
Figure 13: Relationship between normalized Young's modulus, E, (orange bars), normalized shear modulus, G, (black bars)
385 **and normalized porosity (green line) for the studied rock samples.**

4.2 Permeability and UPV measurement at confining pressure

Figure 14 shows the results of permeability, k, and UPV determination under different target confining pressure during
gas permeameter tests. First of all, there is a good agreement between the UPV measurements performed at room pressure
(Figure 8 and Figure 9) and those at the first confining step (0.5 MPa) for each tested sample.

390 As a general pattern, a decrease in permeability and an increase of V_P and V_S are observed at increasing confining
pressures in each specimen. Higher pressures lead therefore to a closure of pores and cracks, and consequently to an
increase of wave velocities, and a decrease of permeability. We note that the permeability of sample AR78 is higher than
all others due to lack of any cement within the collected CFB-FZ specimen also characterized by higher values of porosity
and crack density (cf. Figure 7). Also, considering sample AR12 (CFB-FZ), it shows values of permeability and velocity
395 similar to those documented for AR41 (HR_AFZ) due to cementation processes.
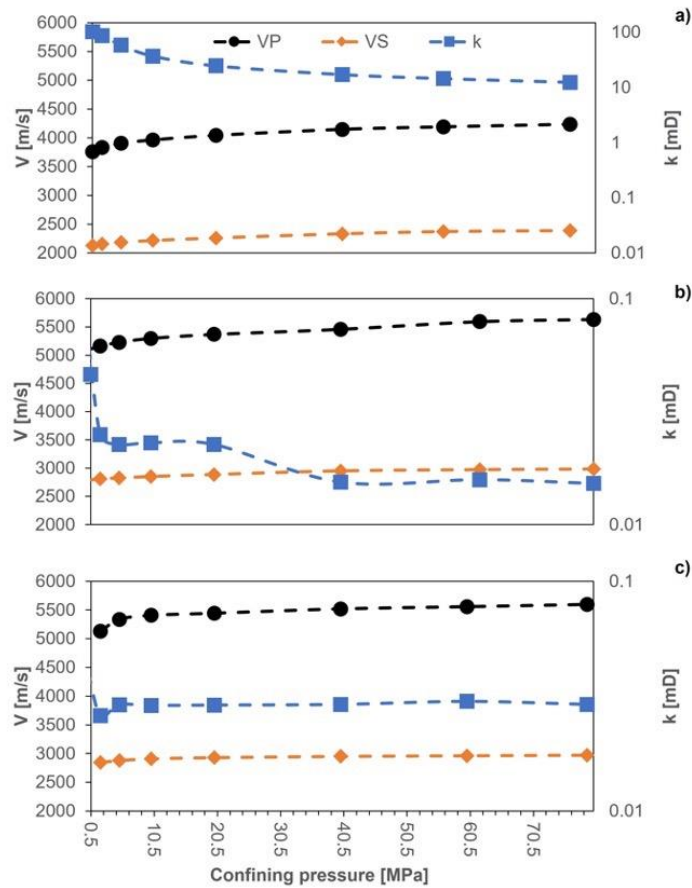
Figure 14: Evolution of permeability (blue symbols), V_P (black symbols) and V_S (orange symbols) as a function of confining pressure during gas permeameter tests on sample a) AR78 (CFB-FZ), b) AR41 (HR-AFZ) and c) AR12 (CFB-FZ).

400 ## 5 Modelling: Elastic properties and crack density

Fluid flow is controlled by the connected network of cracks; consequently, defining the key features describing the crack network geometry such as crack density, size, aspect ratio, and alignment is essential in any attempt of permeability prediction. Gueguen and Dienes (1989) showed that permeability of microcracked rocks can be well represented by that of an array of penny-shaped cracks embedded in an impermeable host matrix. Using the isotropic formulation of their

405 percolation model, the bulk rock permeability, k, can be expressed as follows:

$$k = \frac{2}{15} \cdot f \cdot w^2 \cdot \zeta \cdot \rho \qquad (13)$$

where f is the percolation factor, w is the crack average width, ζ is the average aspect ratio, and ρ is the crack density.

410 Percolation, f, can vary between 0 and 1. When f is equal to 0 it means that all cracks are isolated and unconnected and consequently the rock can be considered as intact with a very low degree of fracturing. Conversely, when f corresponds to the unity, all cracks are connected into the network. Guéguen et al. (1997) showed that the percolation threshold

(defined as the minimum crack density required to establish a complete path for a fluid to flow) for microscopic permeability is reached at values of crack density equals to 0.14. Differently, the percolation threshold for macroscopic fractures is reached at values of crack density close to 1. The percolation factor may be approximated by the connectivity factor, f', as defined by (Gueguen and Dienes, 1989):

$$f' = \frac{9}{4}\left(\frac{\pi^2}{4}\rho - \frac{1}{3}\right) \qquad (14)$$

Since the changes in dynamic elastic properties are correlated to the amount of damage within rocks, it is possible to invert the elastic wave velocity field into a non-dimensional crack density, ρ, as defined by the following equation:

$$\rho = \frac{1}{V}\sum_{i=1}^{N} c_i^3 \qquad (15)$$

where c_i is the radius of the ith crack, and N the total number of cracks embedded in the representative elementary volume V.

The Effective Medium Theory (EMT) introduced the concept of "no stress interaction approximation" by neglecting, as a simple assumption, the stress interactions among cracks. In this case, the effective elastic moduli of a cracked solid can be exactly and rigorously calculated by solely considering crack orientation and distribution (Bristow 1960, Kachanov 1993) . The theory invokes that for cracks randomly oriented and distributed (perfect isotropic configuration), stress interactions are partially geometrically compensated so that the effective Young's modulus, E*, of a dry rock can be obtained as follows:

$$\frac{E_0}{E^*} = 1 + \frac{16\left(1-v_0^2\right)\left(1-\frac{3v_0}{10}\right)}{9\left(1+\frac{v_0}{2}\right)}\rho \qquad (16)$$

where E_0 and v_0 are the Young's modulus and Poisson ratio of the uncracked material, respectively, and E* is the Young's modulus calculated by using the ultrasonic pulse measurements.

The microcrack aspect ratios, ζ, can be also evaluated from results of digital image analysis, as described in Section 3.2, or it may be calculated by simply applying the following equation:

$$\zeta = \frac{<w>}{<2c>} \qquad (17)$$

Recalling that for penny-shaped cracks with constant aspect ratio distribution, the total microcrack porosity, n, is also equal to:

$$n = \pi w c^2 \qquad (18)$$

the aspect ratios, ζ, can be therefore expressed as a function of both porosity, n, and crack density, ζ, as shown by the following equation:

$$\zeta = \frac{n}{2\pi\rho} \qquad (19)$$

In this study, we consider the lithology of the host rock samples distinguishing calcarenites, calcarenitic limestones, micrite limestones, carbonate microbreccias, and carbonate breccias in order to evaluate representative petrological values of E_0 and v_0 by considering maximum values after ultrasonic measurements. Two protocols (workflows, WF) are followed to estimate permeability, k, from seismic measurements. The first one applies the Gueguen and Dienes (1989) and EMT theories; the values of aspect ratio and crack width are after the results of seismic measurements. The second one by assuming a constant crack aperture (width) of 1 μm, which is typical of a crack network geometry. For these two workflows, respectively 1 and 2, the crack density of the analyzed rock blocks is evaluated by inverting equation 16, using E* from seismic measurements, and assuming petrological reference values for E_0 and v_0. Then, the crack aspect ratio is estimated by using eq. 19. In case of workflow 1, once ζ was calculated, the crack average width is obtained from equations 17 and 18. Conversely, following workflow 2, w is considered constant and equal to 1 μm. Finally, k is evaluated by using equation 13; since f is extremely complex to measure, and k is sensitive to its variation, an interval analysis by considering lower and upper limits in the interval of f variation (f equal to 0 and 1) and an intermediate value provided by equation 14 was performed. Moreover, a third workflow employing the results of crack density from digital image analyses is followed.

Figure 15 shows the variation of the calculated permeability values, k, by considering the three aforementioned workflows, and the percolation factors of 0.01 (blue line) and 1 (orange line). Permeability values obtained by considering the percolation factor equals to the connectivity factor (cf. eq. 14) are also reported (grey line). The values of k after experimental work on three samples (cf. Ch. 4.3) at the lowest confining pressure are also reported with black symbols for comparison. In general, the host rock permeability (HR-AFZ, HR-PFZ, FHR-FZ) varies between 0.01 and 10 mD, with a few samples exhibiting k values falling outside this range. Differently, CFB-FZ and FCFB-FZ samples shows higher permeability values up to 100 mD.

For what it concerns the comparison with k values from laboratory tests, the k inferred from seismic measurements (workflow 1) best reproduces the experimental results, especially when percolation factor is evaluated with equation 14 (grey line in Figure 15a). The other workflows mainly miss the higher permeability values (up to 100 mD). Considering workflow 2 (Figure 15b), the calculated permeability values are commonly lower, ranging between 0.001 and 1 mD, with a slight increase for the fault rock samples. The assumption of a constant crack aperture not only determines lower values of calculated permeability, but it also tends to smooth out the differences on permeability. The results obtained by following workflow 3 (Figure 15c), a very slight increase of fault rock permeability with respect to the previous case is documented.
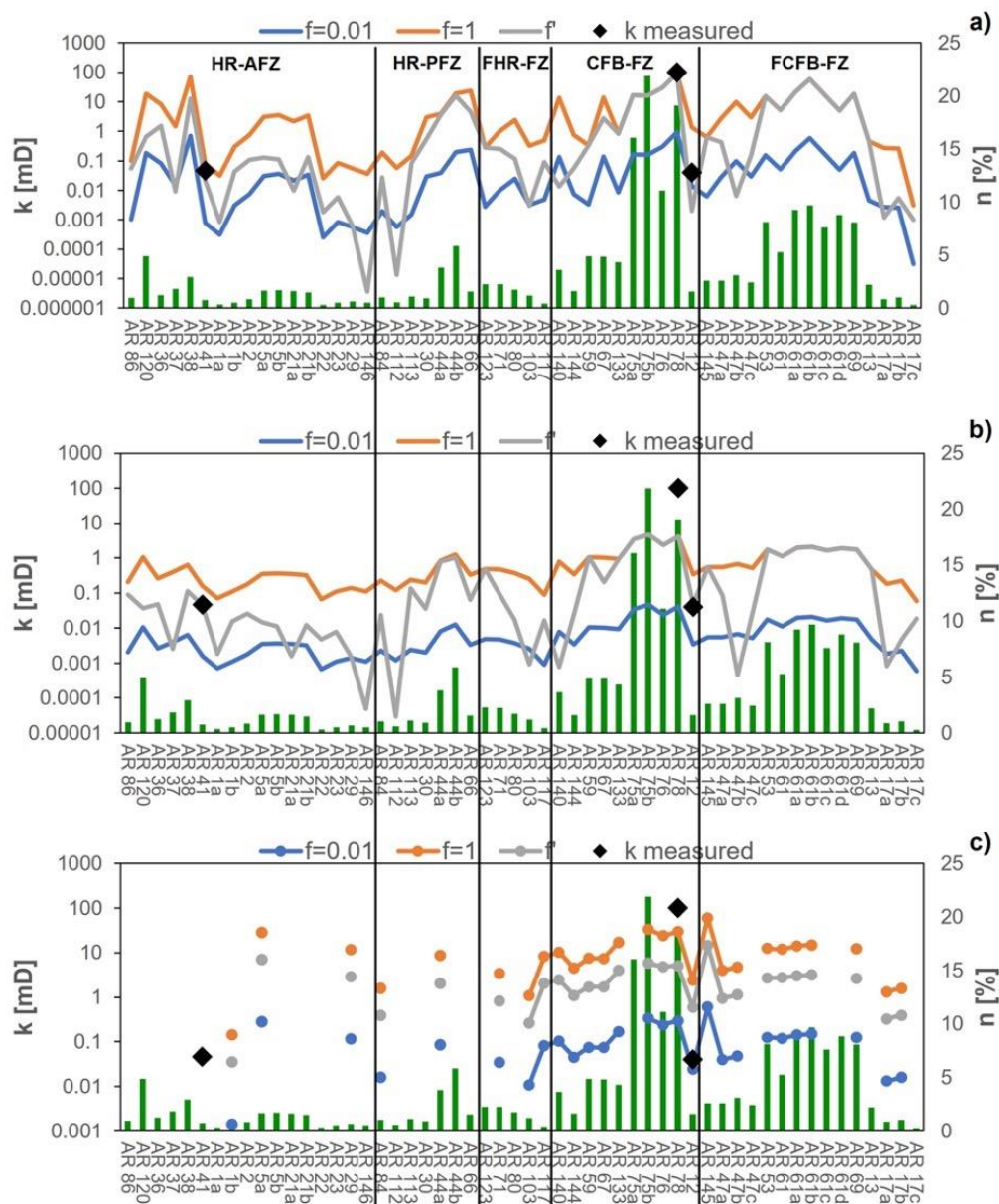
Figure 15: Trend of permeability (orange, grey and blue lines) and porosity (green bars) values evaluated for each rock block by following: a) protocol 1, b) protocol 2, and c) protocol 3. The three reported permeability trends are the results of different 485 percolation factor values: 0.01 for the blue lines, 1 for the orange lines, and estimated by using equation 15 for grey lines. The black diamonds identify the rock block permeability measured with gas permeameter.

490

6   Discussion

We discuss the orginal data in light of the existing bibliography to assess the microscale deformation mechanisms, decipher the type, dimension, and distribution of the pores, and finally establish the poro-perm relations of the studied carbonates.

6.1   Deformation mechanisms

495   The plot $D_{0(grains)}$ vs. % of matrix values obtained after digital images shows a very good fitting ($R^2 = 0.96$) of the data (Figure 16), which is interpreted as due to diffuse fracturing and incipient catclastic processes during anticline folding and faulting of the Araxos Promontory (Bourli et al., 2019a; Smeraglia et al., 2023). In fact, as shown by Ferraro et al. (2018) for the carbonate fault rocks of Italy, evidences for localized chipping and shear fracturing processes associated to grain rolling are not documented due to lack of any sharp change in the slope of the best-fit line. In fact, if present these 500   sharp changes would have produced lower R^2 values. It is also highlighted that the cementation might have coated together the pre-existing survivor grains, obliterating therefore the possible effects of chipping and shear fracturing.
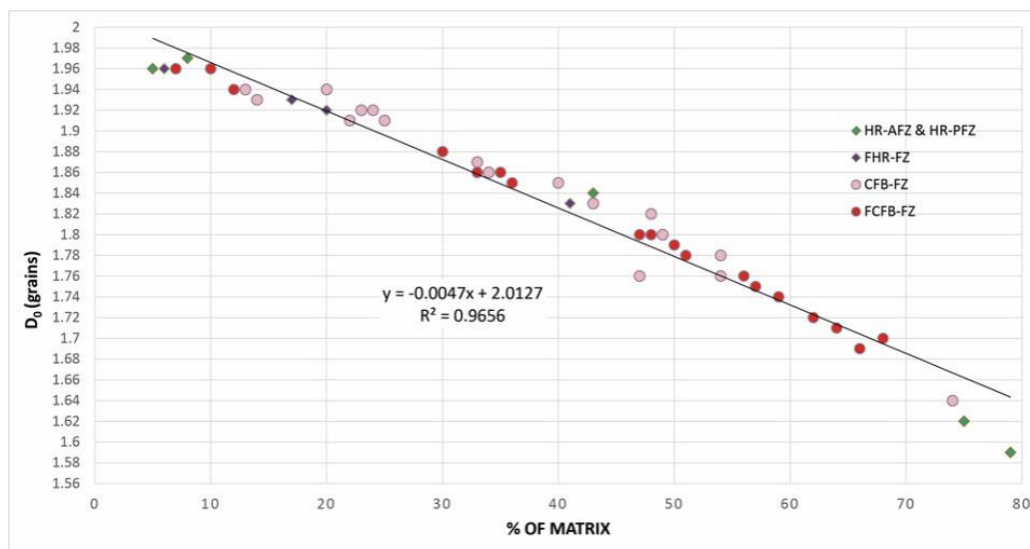
Figure 16: Plots of box-counting Dimension, $D_{0(grain)}$, vs. % of matrix for all host rock and fault-related rock samples.

505   ### 6.2   Pore properties

In order to assess the pore types, we plot the average V_P in dry conditions versus porosity values with respect to the Hashin Strickman upper and lover bounds (HS+ and HS-, respctively), the time-average equation (Wyllie et al., 1958, 1956), and the best fit line proposed by (Anselmetti and Eberli, 2001, 1997, 1993) for carbonates (Figure 17). The HS+, HS-, and time-average equation are calculated for a monimineralic, calcite-rich rock. The former parameters represent 510   the narrowest possible bounds for elastic moduli calculated for an isotropic material by only knowing the volume fractions of the constituents (Mavko et al., 2009), whereas the time-average equation relates the V_P of an isotropic, fluid-saturated, consolidated rock to its porosity assuming that the total travel time can be approximated as the volume-weighted average

of travel times through the individual rock constituents. The best-fit curve predicts the P-wave velocity of carbonates at any given porosity. Values of V_P higher than the best fit are due to presence of molds, which form by selective dissolution

515   on the carbonates not affecting their elastic frame and thus enhancing porosity but not permeability, values lower that the best fit are due to vugs and microfractures.

According to the results (Figure 17), data are consistent with the vast majority of the blocks being affected by vug porosity due to a not-selective dissolution of the carbonates and microfractures. Some of the host rock data points lie along the best fit line, whereas all fault rock data points show presence of vugs/microfractures. Molds are virtually absent. As a

520   comparison, in the latter figure we also report data obtained for large-scale, high-angle carbonate fault zones of central and southern Italy (Ferraro et al., 2020), whic actually shows the effect of some localize dissolution (ie., moldic porosity).
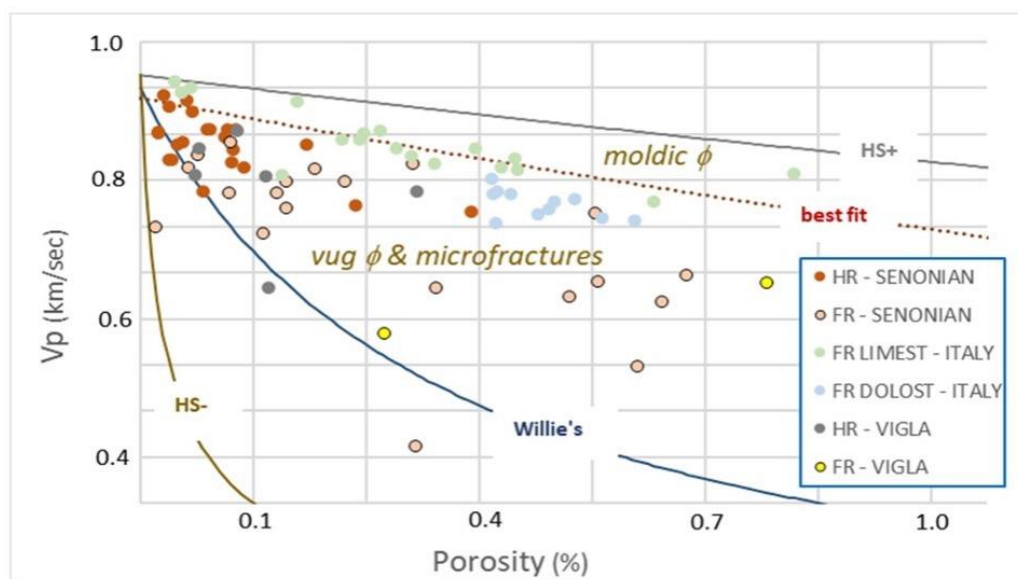
525   **Figure 17: Pore type of carbonate host rocks (HR – SENONIAN, HR – VIGLA) and fault rocks (FR – SENONIAN, FR – VIGLA) deciphered after the comparison between mean Vp (dry) and porosity values. Data normalized to the highest value of porosity, x-axis, and Vp, y-axis. Data points alos include those measured for limestone-hosted (FR LIMEST – ITALY) and dolostone-hosted (FR DOLOST – ITALY) fault rocks from central and southern Italy (Ferraro et al., 2020). The Hashin Strickman upper (H+), and lower bounds (H-), the Willye's time average equation, and the linear best fit equation proposed**

530   **by Eberli and Anselmetti (2001) for carbonates of Italy and Bahamas are also reported. Note that all data points with porosity greater than 14% are not reported in the plot.**

Data obtained after digital image analysis of the pore space characteristics are computed in order to obtain the average, median, and 1σ standard deviation values of both pore aspect ratio (AR) and pore aperture (width, in σm) for host rocks (HR-AFZ, HR-PFZ, FHR-FZ, Table 1), and for fault rocks (CFB-FZ, FCFB-FZ,

535   Table 2). Data are reported for all pores, and for those with aspect ratios ≥ 2 (AR ≥ 2). In both tables, the mean values of median AR and width are in bold; the latter values correspond to the minor axis of the ellipse automatically inscribied within each individual pore.

HR-AFZ & HR-PFZ

	#	ASPECT RATIO						WIDTH (μm)					
		whole image			AR > 2			whole image			AR > 2		
		AR average	AR median	AR st dev	AR average	AR median	AR st dev	WIDTH average	WIDTH median	WIDTH st dev	WIDTH average	WIDTH median	WIDTH st dev
SENONIAN WACKEST ONE	AR 1 P		**1,52**			**2,18**			**1,13**			**2,67**	
	1	1,66	1,52	0,74	2,43	2,18	0,58	9,7	1,13	37,96	18,9	2,67	61,89
	2												
SENONIAN MUDSTON E	AR 5		**2,985**			**3,9**			**8,935**			**11,97**	
	1	2,5	1,68	1,59	3,54	3,08	1,57	6,9	2,67	7,31	11,6	8,94	3,95
	2	4,88	4,29	3,24	5,35	4,72	3,2	8,6	15,2	11,5	16,5	15	9,42
SENONIAN BRECCIA	AR 29		**2,715**			**4,54**			**9,12**			**13,95**	
	1	4,6	2,8	4,65	6,56	5,33	4,89	21,6	11,8	25,5	20.04	15,7	18,2
	2	3,55	2,63	3,14	5,04	3,75	3,19	11,8	6,44	13,8	15	12,2	12,4
SENONIAN BRECCIA	AR 44 c		**1,285**			**2,49**			**3,245**			**3,355**	
	1	1,81	1,57	0,92	2,68	2,59	0,89	10,5	3,82	19,5	11	4,04	20,4
	2	1,51	1	0,9	2,7	2,39	0,98	4,28	2,67	5,51	5,43	2,67	7,25
VIGLA PACKSTON E	AR 84		**1,51**			**2,535**			**2,67**			**3,765**	
	1	1,96	1,47	2,09	3,14	2,42	2,94	6,12	2,67	8,91	7,43	3,75	10,4
	2	1,96	1,55	1,41	3,09	2,65	1,68	7,63	2,67	11,7	8,47	3,78	12,2
VIGLA MUDSTON E	AR 84 Bis		**16,52**			**16,52**			**39,7**			**39,7**	
	1	5,37	4,68	2,32	5,37	4,68	2,32	51,2	56,5	18,3	51,2	56,5	18,3
	2	28,36	28,36	20,77	28,36	28,36	20,77	22,9	22,9	14,8	22,9	22,9	14,8

FHR-FZ

	#	ASPECT RATIO						WIDTH (μm)					
		whole image			AR > 2			whole image			AR > 2		
		AR average	AR median	AR st dev	AR average	AR median	AR st dev	WIDTH average	WIDTH median	WIDTH st dev	WIDTH average	WIDTH median	WIDTH st dev
VIGLA FR. MUDSTON E	AR 71		**1,23**			**2,48**			**2,67**			**3,075**	
	1	1,63	1	1,43	2,77	2,31	2,09	4,64	2,67	28,6	7,69	2,67	50,4
	2	1,99	1,46	2,54	3,63	2,65	3,9	7,85	2,67	25,9	12,7	3,48	36,3
SENONIAN FR. MUDSTON E	AR 103		**1,45**			**2,555**			**2,06**			**2,47**	
	1	2,16	1,45	2,94	4,02	2,54	4,45	8,31	1,45	2,94	12,6	3,75	20,4
	2	1,62	1,45	0,74	2,54	2,57	0,55	10,4	2,67	60,7	15,6	1,19	35,44
SENONIAN BRECCIA	AR 117		**3,015**			**3,545**			**9,585**			**9,585**	
	1	1,72	1,59	0,77	2,48	2,65	0,41	21,4	2,67	55,8	28,9	2,67	73,6
	2	5,12	4,44	2,78	5,12	4,44	2,78	18,8	16,5	6,62	18,8	16,5	6,62

540

Table 1: Summary of the main pore characteristics (Aspect Ratio, AR, and Width, in σm) computed for the samples collected either away from or in proximity to meso-scale fault zones. The aforementioned characteristics are reported for all of the pores depicted in the whole images, and for pores with AR > 2. Numbers in bold represent the mean values computed for single thin sections.

CFB-FZ

#	ASPECT RATIO						WIDTH (µm)					
	whole image			AR > 2			whole image			AR > 2		
	AR average	AR median	AR st dev	AR average	AR median	AR st dev	WIDTH average	WIDTH median	WIDTH st dev	WIDTH average	WIDTH median	WIDTH st dev
AR 12 V		1,23			2,075			2,67			2,67	
1	1,52	1	0,66	2,36	2	0,5	3,59	2,67	2,25	3,47	2,67	2,84
2	1,63	1,46	0,71	2,42	2,15	0,59	3,95	2,67	2,73	3,67	2,67	1,88
AR 59 V		1,23			2,475			2,67			3,095	
1	1,63	1	0,91	2,65	2,48	0,89	4,54	2,67	8,2	5,25	2,67	3,67
2	1,7	1,46	0,9	2,7	2,47	0,87	15,3	2,67	43	14,3	3,52	37,4
AR 67b V		1,43			2,635			2,67			2,74	
1	1,89	1,57	1,15	2,82	2,65	1,19	5,21	2,67	9,94	5,48	2,81	11,9
2	1,7	1,29	0,95	2,66	2,62	0,88	4,34	2,67	12,1	4,36	2,67	11,6
AR 75b V		1,535			2,65			2,67			2,905	
1	1,9	1,46	1,27	2,95	2,65	1,3	4,49	2,67	11,1	4,95	2,69	8,82
2	1,97	1,61	1,26	2,97	2,65	1,31	5,37	2,67	18,9	5,15	3,12	7,03
AR 76_1 V		1,27			2,595			3,175			3,4	
1	1,81	1,54	1,02	2,76	2,54	1,07	8,51	3,68	27,8	11,5	3,78	43,1
2	1,68	1	1,14	2,91	2,65	1,35	5,77	2,67	19,7	9,43	3,02	34,3
AR 76_2 V		1,355			2,63			2,67			2,74	
1	1,71	1,21	0,95	2,66	2,61	0,88	4,22	2,67	7,88	4,47	2,67	8,71
2	1,83	1,5	1,04	2,79	2,65	1	6,45	2,67	18,9	7,08	2,81	25,9
AR 78 V		1,315			2,47			2,685			3,15	
1	1,61	1	0,96	2,65	2,39	1,1	5,91	2,67	15,3	6,28	2,67	15,5
2	1,93	1,63	1,19	2,88	2,55	1,26	8,1	2,7	25	7,32	3,63	15,4
AR 133 V		1,515			3,01			4,28			5,225	
1	3,96	1,74	4,7	7,47	3,4	5,43	25,1	5,89	55,15	21,1	7,78	33,66
2	1,7	1,29	0,95	2,66	2,62	0,88	4,34	2,67	12,1	4,36	2,67	11,6
AR 140 V		1,575			2,63			3,635			3,795	
1	1,77	1,55	0,9	2,7	2,61	0,86	8,28	3,82	21,6	11,3	3,78	33,8
2	2,03	1,6	1,52	3,12	2,65	1,78	7,54	3,45	17,5	7,86	3,81	17,2
AR 144a V		1,745			3,29			3,605			3,73	
1	4,27	2,49	3,76	5,63	3,93	3,79	10,39	4,54	19,45	6,35	4,65	3,97
2	2,03	1	2,6	3,6	2,65	3,76	5,78	2,67	14,5	8,43	2,81	20,4
AR 144b V		1			2,65			2,67			2,31	
1	1,26	1	0,58	2,55	2,65	0,49	3,23	2,67	3,84	2,63	2,31	0,6
2												

CFB-FZ

#	ASPECT RATIO						WIDTH (µm)					
	whole image			AR > 2			whole image			AR > 2		
	AR average	AR median	AR st dev	AR average	AR median	AR st dev	WIDTH average	WIDTH median	WIDTH st dev	WIDTH average	WIDTH median	WIDTH st dev
AR 17a		1,425			2,665			2,67			2,74	
1	1,98	1,85	1,13	2,84	2,65	1,07	4,67	2,67	2,3	4,6	2,81	4,89
2	2,27	1	2,95	4,6	2,68	4,1	4,43	2,67	5,6	7,46	2,67	8,71
AR 17b		1,23			2,25			2,67			2,74	
1	1,63	1	1,27	2,65	2,32	1,77	3,89	2,67	5,,56	4,56	2,67	8,01
2	1,67	1,46	1,01	2,62	2,18	1,24	5,23	2,67	3,1	6,31	2,81	10,8
AR 47a		1,465			2,65			2,67			2,74	
1	1,75	1,47	0,91	2,65	2,65	0,81	4,93	2,67	13,38	4,82	2,67	13,1
2	1,76	1,46	0,94	2,75	2,65	0,75	11,8	2,67	27,7	17,9	2,81	37,8
AR 47b		1,5			2,54			2,67			2,67	
1	1,91	2	1,04	2,75	2,65	0,8	10,7	2,67	58,5	16,2	2,67	80,6
2	1,59	1	0,96	2,7	2,43	1,11	15,6	2,67	92	18,3	2,67	78,1
AR 53		1,465			2,7			2,67			4,13	
1	1,99	1,67	1,14	2,96	2,7	1,01	12,1	2,67	43	20,9	3,07	62
2	2,06	1,26	2,14	3,73	2,7	2,92	19	2,67	55,5	24,9	5,19	66,3
AR 61		1,505			2,47			3,245			3,47	
1	1,73	1,46	1,14	2,71	2,45	1,45	7,53	2,67	18,4	8,26	3,02	22,7
2	1,93	1,55	1,67	3	2,49	2,31	13	3,82	32,2	10,9	3,92	18,8
AR 61penta_a		1,465			2,38			2,67			2,81	

1	1,72	1,46	1,21	2,74	2,35	1,57	5,65	2,67	11,8	6,18	2,81	12,4
2	1,72	1,47	0,84	2,58	2,41	0,76	5,67	2,67	12	6,14	2,81	13,5
AR												
61penta_b		**1,5**			**2,39**			**2,67**			**3,2**	
1	1,73	1,46	1,22	2,68	2,32	1,59	6,41	2,67	26,7	7,36	2,81	27,4
2	1,75	1,54	0,87	2,6	2,46	0,83	6,58	2,67	17,5	6,06	3,59	12,2
AR 69		**1,235**			**2,35**			**2,67**			**2,74**	
1	1,55	1	0,82	2,52	2,3	0,84	4,28	2,67	9,81	5,5	2,67	16,2
2	1,74	1,47	1,21	2,67	2,4	1,59	6,18	2,67	16,8	7,35	2,81	25,5
AR 145		**1,6**			**2,305**			**10,41**			**4,4**	
1	1,67	1,46	0,74	2,56	2,3	0,69	18,6	3,82	65,4	33,8	2,84	111
2	1,81	1,74	0,51	2,31	2,31	0,34	61,8	17	108	7,71	5,96	5,97

545

Table 2: Summary of the main pore characteristics (Aspect Ratio, AR, and Width, in □m) computed for the fault breccia and fine crush fault breccia and fault microbreccia samples collected from meso-scale fault zones. The aforementioned characteristics are reported for all of the pores depicted in the whole images, and for pores with AR > 2. Numbers in bold represent the mean values computed for single thin sections.

550 The pore volume distribution in carbonates can be fractal (Wu et al., 2019, and references therein), and statistically described by a power-law function (Mandelbrot, 1985). If the spatial pattern of the pores is also fractal, the plot of the box size versus the filling frequency is power-law, and corresponds to the angular coefficient of the best fit line ($D_{0(pores)}$, Falconer, 2003; Ferraro et al., 2018). Considering $D_{0(pores)}$ vs. $2D\varphi$ (Figure 18), they show a positive correlation. $D_{0(pores)}$ increases with higher $2D$ φ, meaning that pores are more uniformly distributed in higher porosity carbonates, which

555 correspond to fault rocks. The very low value of the fitting coefficient ($R^2 = 0.25$, Figure 18) is due to outliers likely associated to the effect of not-selective dissolution of the carbonates, which affected both host rocks and fault rocks.
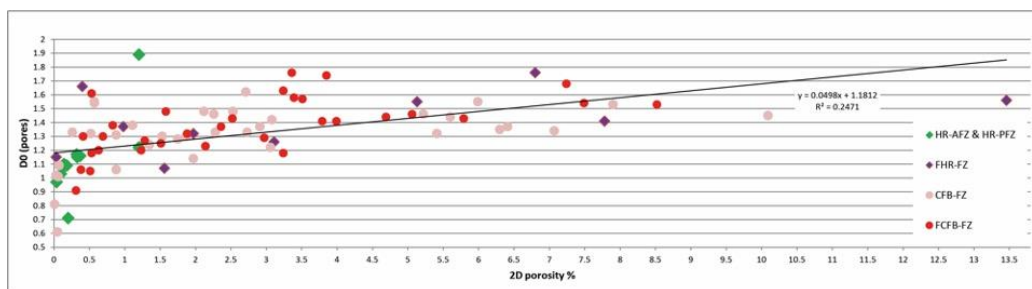
Figure 18: $D_{0(pores)}$ vs. % of 2D porosity for all rocks.

6.3 Poro-perm relations

560 The poro-perm relations are assessed by considering the connectivity factor, f', employed for the workflow 1, as reported in Section 5. As shown in Figure 19, the carbonate host rocks (HR-AFZ, HR-PFZ, FHR-FZ) do not show any significant poro-perm relation. In fact, the calculated k values exhibit a large permeability variation, up to. 4 orders of magnitude, and do not vary proportionally with porosity.
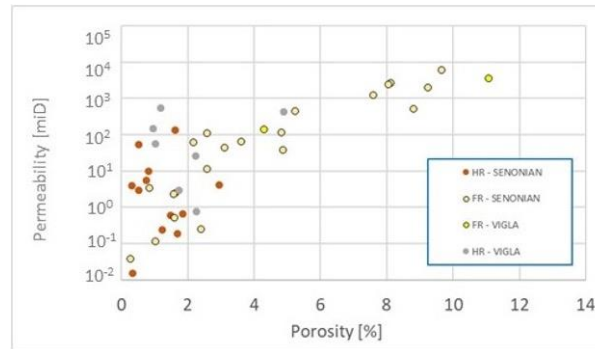
565

Figure 19: Poro-perm relations for both host rocks (HR – SENONIAN, HR – VIGLA) and fault rocks (FR – SENONIAN, FR – VIGLA) considering the connectivity factor, f', and adopting workflow (1). We note that 1 Darcy ~ 9.8*10⁻¹³m². All data points with porosity greater than 14% are not reported in the plot.

This lack of relation can be explained by considering the presence of stiff, sub-rounded pores in some of the host rock

570   blocks, and of vugs/microfractures in others (Agosta et al, 2007; Ferraro et al., 2020). On the contrary, although the fault rocks (CFB-FZ and FCFB-FZ) show a very large permeability variation, up to ca. 5 order of magnitude, the calculated k values linearly increase with porosity. This linear relation is interpreted as due to a connected pore network (Ehrenberg et al., 2006), which is made of vugs/microfractures (cf. Ch. 6.2). Such a linear poro-perm relation is therefore supporting previous interpretations after experimental works on cohesive rocks (Benson et al., 2006; Nasseri et al., 2007), which

575   concluded that seismic data obtained via geophysical surveys are suitable for permeability calculations.

Finally, the behavior of permeability evaluated by considering the connectivity factor is also shown with respect to values of porosity (Figure 20a). There, the qualitative trend (dashed line) shows a general increase of permeability that mirrors that of porosity, as confirmed by observing the relation between crack density and porosity (Figure 20b).
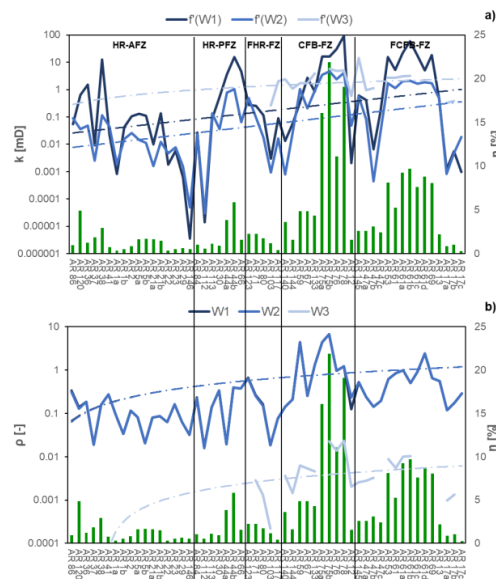
580

Figure 20. Comparison among the a) k values estimated from W1 to W3, b) crack density and porosity for each analyzed rock block. The dash-dotted lines represent the general trends deciphered for each workflow.

7 Conclusions

We present the results of a petrophysical characterization of Mesozoic carbonate rocks collected from outcrops of the Araxos Promontory, northwest Greece, in order to define the poro-perm relation of both host rocks and fault rocks. Rock samples consist of Senonian and Vigla formations made of carbonate mudstones, wackestones, packstones and sedimentary breccias, and of fault breccias collected from high-angle extensional and strike-slip fault zones. With respect to the host rocks, results showed that the fault breccias are characterized by a wider range of density, up to 5-10 times greater porosity, and lower ultrasonic velocities. A slight textural anisotropy is documented in the carbonate host rocks, whereas a more evident anisotropy characterizes the fault rocks mirroring the increase of porosity. Independently on lithology, the carbonate host rocks include small vugs, wherea the fault breccia also include microfractures. Selected samples were also tested in pressure vessels with confining pressure up to 80MPa, showing that transport properties along microcracks in fault breccias can significantly increase with increasing depth.

In order to compute the poro-perm relations, three different protocols were employed to compute permeability: i) under the hypotheses of the Effective Medium Theory, the results of ultrasonic measurements were considered, ii) a constant crack aperture of 1 μm was applied, and iii) crack density values after 2D image analysis were used. The results highlighted that the carbonate host rocks did not show a clear poro-perm trend due to the presence of stiff, sub-rounded pores and of small vugs. The fault breccia showed a linearly increase of permeability with porosity due to a connected pore network including microfractures. Regarding the employed protocols, the first two showed variations of permeability with porosity, whereas the third one did not exhibit systematic variation due to the wide range of fracture aperture values caused by not-selective dissolution of the outcropping carbonates. Overall, a good correspondence between theoretical calculations after application of the first protocol and gas permeability measurements was observed.

Competing interests

The contact author has declared that none of the authors has any competing interests.

Acknowledgements

Scientific discussion with C. Turrini and E. Panza is acknowledged. We thank S. Grimaldi and C. Manniello for the help provided during fieldwork activities. Financial support from Hellenic Petroleum is acknowledged. Fieldwork activities and laboratory analyses were also supported by the Reservoir Characterization Project (www.rechproject.com).

References

Agosta, F. and Aydin, A.: Architecture and deformation mechanism of a basin-bounding normal fault in Mesozoic platform carbonates, central Italy, J. Str. Geo., 28, 1445–1467, 2006.

Agosta, F., Prasad, M. and Aydin, A.: Physical properties of carbonate fault rocks, Fucino basin (central Italy): implications for fault seal in platform carbonates, Geofluids, 7, 19–32, 2007.

Agosta, F., Manniello, C., Cavalcante, F., Belviso, C. and Prosser, G.: Late Cretaceous transtensional faulting of the Apulian Platform, Italy, Mar. Pet. Geo., 127, 104889, 2021.

Anselmetti, F.S. and Eberli, G.P.: Sonic Velocity in Carbonate Sediments and Rocks, in: Carbonate Seismology. Society of Exploration Geophysicists, 53–74, https://doi.org/10.1190/1.9781560802099, 1997.

Anselmetti, F.S. and Eberli, G.P.: Sonic velocity in carbonates - a combined product of depositional lithology and diagenetic alteration, in: Subsurface Geology of a Prograding Carbonate Platform Margin Great Bahama Bank. Soc. Sed. Geo., 193–216. https://doi.org/10.2110/pec.01.70.0193, 2001.

Anselmetti, F.S. and Eberli, G.P.: Controls on sonic velocity in carbonates, Pur. App. Geo., 141, 287–323, https://doi.org/10.1007/BF00998333, 1993.

ASTM D2845-08, Standard Test Method for Laboratory Determination of Pulse Velocities and Ultrasonic Elastic Constants of Rock. ASTM, International (Ame. Soc. Test. Mat.), West Conshohocken, Pennsylvania, USA, 2008.

Bailly, C., Adelinet, A., Hamon, Y. and Fortin, J.: Combined controls of sedimentology and diagenesis on seismic properties in lacustrine and palustrine carbonates (Upper Miocene, Samos Island, Greece), Geo. J. Int. 219 (2), 1300-1315, 2019a.

Bailly, C., Fortin, J., Adelinet, M. and Hamon Y.: Upscaling of elastic properties in carbonates: A modeling approach based on a multiscale geophysical data set, J. Geo. Res.: Sol. Ear., 124 (12), 13021-13038, 2019b.

Bailly, C., Kernif, T., Hamon, Y., Adelinet, M. and Fortin J.: Controlling factors of acoustic properties in continental carbonates: Implications for high-resolution seismic imaging, Mar. Pet. Geo., 137, 105518, 2022.

Benson, P., Schubnel, A., Vinciguerra, S., Trovato, C., Meredith, P. and Young, R.P.: Modeling the permeability evolution of microcracked rocks from elastic wave velocity inversion at elevated isostatic pressure., J. Geo. Res 111, B04202, https://doi.org/10.1029/2005JB003710, 2006.

Bourli, N., Pantopoulos, G., Maravelis, A. G., Zoumpoulis, E., Iliopoulos, G., et al.: Late Cretaceous to early Eocene geological history of the eastern Ionian Basin, southwestern Greece: a sedimentological approach, Cre. Res., 98, 47-71. 2019a.

Bourli, N., Kokkaliari, M., Iliopoulos, I., Pe-Piper, G., Piper, D.J., Maravelis, A.G., and Zelilidis, A.: Mineralogy of siliceous concretions, cretaceous of ionian zone, western Greece: Implication for diagenesis and porosity, Mar. Pet. Geo., 105, 45-63, 2019b.

Bristow: Microcracks and the static and dynamic elastic constants of annealed and heavily cold-worked metals. Brit. J. App. Phys, 11:81, 1960.

Chatzaras, V., Xypolias, P. and Doutsos, T.: Exhumation of high-pressure rocks under continuous compression: a working hypothesis for the southern Hellenides (central Crete, Greece), Geol. Mag. 143, 859–876. https://doi.org/10.1017/S0016756806002585, 2006.

Danelian, T., Bonneau, M., Cadet J. P., Poisson, A., Vrielynck, B.: Palaeoceanographic implications of new and revised bio-chronostratigraphic constraints from the Profitis Ilias Unit (Rhodes, Greece). Bul. Geol. Soc. of Gre. 34, 619. https://doi.org/10.12681/bgsg.17111, 2018.

Doutsos, T., Pe-Piper, G., Boronkay, K. and Koukouvelas, I.: Kinematics of the central Hellenides, Tect. 12, 936–953. https://doi.org/10.1029/93TC00108, 1993.

Ehrenberg, S.N., Eberli, G.P., Keramati, M. and Moallemi, S.A.: Porosity-permeability relationships in interlayered limestone-dolostone reservoirs, Am Assoc Pet Geol Bull 90, 91–114. https://doi.org/10.1306/08100505087, 2006.

Falconer, K.: Fractal Geometry: Mathematical Foundations and Applications. John Wiley and Sons, London, United Kingdom, 400, 2003.

655 Ferraro, F., Agosta, F., Prasad, M., Vinciguerra, S., Violay, M. and Giorgioni, M.: Pore space properties in carbonate fault rocks of peninsular Italy. J. Struct. Geol. 130, 10391, 2020

Ferraro, F., Grieco, D.S., Agosta, F. and Prosser, G.: Space-time evolution of cataclasis in carbonate fault zones. J. Struct. Geol. 110, 45–64, 2018.

Giuffrida, A., La Bruna, V., Castelluccio, P., Panza, E., Rustichelli, A., Tondi, E., Giorgioni, M. and Agosta, F.: Fracture
660 simulation parameters of fractured reservoirs: analogy with outcropping carbonates of the Inner Apulian Platform. southern Italy. J. Str. Geol. 123, 18–41, 2019.

Guéguen, Y., Chelidze, T. and Le Ravalec, M.: Microstructures, percolation thresholds, and rock physical properties. Tectonophysics 279, 23–35. https://doi.org/10.1016/S0040-1951(97)00132-7, 1997.

Gueguen, Y. and Dienes, J., Transport properties of rocks from statistics and percolation. Math Geol 21, 1–13.
665 https://doi.org/10.1007/BF00897237, 1989.

ISRM, Commission on standardization of laboratory and field tests, suggested methods for determining water content, porosity, density, absorption and related properties and swelling and slake durability index properties. Int. J. Rock Mech. Min. Sci. Geom. Abstr. 16, 141–156, 1979.

Jolivet, L. and Brun, J.-P.: Cenozoic geodynamic evolution of the Aegean, Int. J. Ear. Sci. 99, 109–138.
670 https://doi.org/10.1007/s00531-008-0366-4, 2010.

Jolivet, L., Menant, A., Sternai, P., Rabillard, A., Arbaret, L., Augier, R., Laurent, V., Beaudoin, A., Grasemann, B., Huet, B., Labrousse, L. and Le Pourhiet, L.: The geological signature of a slab tear below the Aegean, Tectonop., 659, 166–182. https://doi.org/10.1016/j.tecto.2015.08.004, 2015.

Kachanov, M.: Elastic solids with many cracks and related problems, Adv. App. Mec., 30, 259:445, 1993.
675 Karakitsios, V.: Western Greece and Ionian Sea petroleum systems, Am. Ass. Pet. Geol. Bull. 97, 1567–1595. https://doi.org/10.1306/02221312113, 2013.

Karakitsios, V. and Rigakis, N.: Evolution and petroleum potential of Western Greece. Journal of Petroleum Geology 30, 197–218, https://doi.org/10.1111/j.1747-5457.2007.00197.x, 2007.

Kiratzi, A. and Louvari, E.: Focal mechanisms of shallow earthquakes in the Aegean Sea and the surrounding lands
680 determined by waveform modelling: a new database. J Geodyn 36, 251–274. https://doi.org/10.1016/S0264-3707(03)00050-4, 2003.

Laubach, S.E., Eichhubl, P., Hilgers, C. and Lander, R.H.: Structural diagenesis, J. Struct. Geol, 32, 1866–1872, 2010.

Lucia, F.J.: Carbonate Reservoir Characterization: an Integrated Approach, second ed. Springer-Verlag Berlin Heid. Springer editor, 336 pp. https://doi.org/10.1007/978-3-540-72742-2, 2007.

685 Mandelbrot, B.B.: Self-affine fractals and fractal dimension, Phys. Scri., 32, 257–260, 1985.

Mavko, G., Mukerji, T., and Dvorkin, J.: The Rock Physics Handbook. Cambridge University Press. https://doi.org/10.1017/CBO9780511626753, 2009.

Mountrakis, D.: The Pelagonian Zone in Greece: A Polyphase-Deformed Fragment of the Cimmerian Continent and Its Role in the Geotectonic Evolution of the Eastern Mediterranean. J Geol 94, 335–347. https://doi.org/10.1086/629033,
690 1986.

Nasseri, M.H.B., Schubnel, A. and Young, R.P.: Coupled evolutions of fracture toughness and elastic wave velocities at high crack density in thermally treated Westerly granite. International Journal of Rock Mechanics and Mining Sciences 44, 601–616. https://doi.org/10.1016/J.IJRMMS.2006.09.008, 2007.

Nelson, R.A.: Geologic Analysis of Naturally Fractured Reservoirs, second ed. Gulf Prof. Pub., Woburn, 2001.

695   Papanikolaou, D.I.: The Geology of Greece. Spr. I. Pub., Cham. https://doi.org/10.1007/978-3-030-60731-9, 2021.

Piscopo, V., Baiocchi, A., Lotti, F., Ayan, E.A., Biler, A.R., Ceyhan, A.H., Cüylan, M., Dişli, E., Kahraman, S. and Taşkın, M.: Estimation of rock mass permeability using variation in hydraulic conductivity with depth: experiences in hard rocks of western Turkey. Bul. Eng. Geo. Env. 77, 1663–1671. https://doi.org/10.1007/s10064-017-1058-8, 2018.

Rawling, G.C., Goodwin, L.B. and Wilson, J.L.: Internal architecture, permeability structure, and hydrologic significance
700   of contrasting fault-zone types. Geol. 29, 43. https://doi.org/10.1130/0091-7613, 2001.

Robertson, A. and Shallo, M.: Mesozoic–Tertiary tectonic evolution of Albania in its regional Eastern Mediterranean context. Tectonophysics 316, 197–254. https://doi.org/10.1016/S0040-1951(99)00262-0, 2000.

Robertson, A.H.F., Clift, P.D., Degnan, P.J. and Jones, G.: Palaeogeographic and palaeotectonic evolution of the Eastern Mediterranean Neotethys, Palaeogeog. Palaeoclim. Palaeoecol., 87, 289–343, https://doi.org/10.1016/0031-
705   0182(91)90140-M, 1991.

Robertson, A.H.F. and Dixon, J.E.: Introduction: aspects of the geological evolution of the Eastern Mediterranean. Geological Society, London, Special Publications 17, 1–74. https://doi.org/10.1144/GSL.SP.1984.017.01.02, 1984.

Roure, F., Fili, I., Nazaj, S., Cadet, J.-P., Mushka, K. and Bonneau, M.: Kinematic Evolution and Petroleum Systems— An Appraisal of the Outer Albanides, in: Thrust Tectonics and Hydrocarbon Systems. Ame. Ass. Petr. Geo., 485–504.
710   https://doi.org/10.1306/M82813C25, 2004

Saccani, E., Padoa, E. and Photiades, A.: Triassic mid-ocean ridge basalts from the Argolis Peninsula (Greece): new constraints for the early oceanization phases of the Neo-Tethyan Pindos basin, Geo. Soc., London, Spec. Pub. 218, 109–127, https://doi.org/10.1144/GSL.SP.2003.218.01.07, 2003

Sammis, C.G., King, G. and Biegel, R.: The kinematics of gouge deformation. Pure Appl. Geophys, 125, 777–812, 1987.

715   Simmons, G. and Cooper, H.W.: Thermal cycling cracks in three igneous rocks. Int. J. Roc. Mech. and Min. Sci. & Geo. Abstracts 15, 145–148. https://doi.org/10.1016/0148-9062(78)91220-2, 1987.

Skourtsis-Coroneou, V., Solakius, N. and Constantinidis, I.: Cretaceous stratigraphy of the Ionian Zone, Hellenides, western Greece, Cret. Res 16, 539–558. https://doi.org/10.1006/CRES.1995.1035, 1995.

Smeraglia, L., Bernasconi, S., Manniello, C., Spanos, D., Pagoulatos, A., Aldega, L., Kylander-Clark, A., Jaggi, M. and
720   Agosta, F. 2023: Regional scale, fault-related fluid circulation in the Ionian Zone of the External Hellenides fold-and-thrust belt, western Greece: clues for fluid flow in fractured carbonate reservoirs: Tectonics, 42, e2023TC007867. https://doi.org/10.1029/2023TC007867.

Sotiropoulos, S., Kamberis, E., Triantaphyllou, M. V. and Doutsos, T.: Thrust sequences in the central part of the External Hellenides. Geol Mag 140, 661–668, https://doi.org/10.1017/S0016756803008367, 2003.

725   Stampfli G. M.: Plate tectonic of the Apulia-Adria microcontinents., in: Finetti I. R. (Ed.), CROP PROJECT Deep Seismic Exploration of the Mediterranean and Italy. Elsevier, 747–766, 2005.

Tavani, S., Corradetti, A., De Matteis, M., Iannace, A., Mazzoli, S., Castelluccio, A., Spanos, D., and Parente, M.: Early-orogenic deformation in the Ionian zone of the Hellenides: Effects of slab retreat and arching on syn-orogenic stress evolution, J. Str. Geo., 124, 168-181, 2019

730   Thompson, A.H., 1991: Fractals in rock physics. Ann. Rev. Ear. Pla. Sci. 19, 237–262, 1991

Underhill, J.R.: Late Cenozoic deformation of the Hellenide foreland, western Greece, Geol. Soc. Am. Bul., 101, 613–634, https://doi.org/10.1130/0016-7606(1989)101<0613:LCDOTH>2.3.CO;2, 1989.

Volatili, T., Agosta, F., Cardozo, N., Zambrano, M., Lecomte, I. and Tondi, E.: Outcrop-scale fracture analysis and seismic modelling of a basin-bounding normal fault in platform carbonates, central Italy, J. Struct. Geol., 155, 104515,
735   2022.

Walsh, J.B.: The effect of cracks on the compressibility of rock., J. Geo. Res., 70, 381–389. https://doi.org/10.1029/JZ070i002p00381, 1965.

Woodcock, N. H and Mort, K.: Classification of fault breccias and related fault rocks, Geol. Mag. 145, 435–440, 2008.

Wu, J., Fan, T., Rivas, E.G., Gao, Z., Yao, S., Li, W., Zhang, C., Sun, Q., Gu, Y. and Xiang, M.: Impact of pore structure
740   and fractal characteristics on the sealing capacity of Ordovician carbonate cap rock in the Tarim Basin, China. Mar. Pet. Geol. 102, 557–559, 2019.

Wyllie, M.R.J., Gregory, A.R. and Gardner, G.H.F.: An experimental investigation of factors affecting elastic wave velocities in porous media, Geophysics, 23, 459–493, https://doi.org/10.1190/1.1438493, 1958.

Wyllie, M.R.J., Gregory, A.R. and Gardner, L.W.: Elastic wave velocity in heterogeneous and porous media. Geophysics,
745   21, 41–70, https://doi.org/10.1190/1.1438217, 1956

Xypolias, P. and Koukouvelas, I.: Paleostress magnitude in a fold-thrust belt (External Hellenides, Greece): evidence from twinning in calcareous rocks, Episodes 28, 245–251. https://doi.org/10.18814/epiiugs/2005/v28i4/002, 2005.

Fare clic o toccare qui per immettere il testo.